



**HAL**  
open science

## Petrogenesis of martian sulfides in the Chassigny meteorite

Jean-Pierre Lorand, Sylvain Pont, Vincent Chevrier, Ambre Luguët, Brigitte Zanda, Roger Hewins

► **To cite this version:**

Jean-Pierre Lorand, Sylvain Pont, Vincent Chevrier, Ambre Luguët, Brigitte Zanda, et al.. Petrogenesis of martian sulfides in the Chassigny meteorite. *The American Mineralogist*, 2018, 103 (6), pp.872-885. 10.2138/am-2018-6334 . hal-02183086

**HAL Id: hal-02183086**

**<https://hal.science/hal-02183086>**

Submitted on 15 Jul 2019

**HAL** is a multi-disciplinary open access archive for the deposit and dissemination of scientific research documents, whether they are published or not. The documents may come from teaching and research institutions in France or abroad, or from public or private research centers.

L'archive ouverte pluridisciplinaire **HAL**, est destinée au dépôt et à la diffusion de documents scientifiques de niveau recherche, publiés ou non, émanant des établissements d'enseignement et de recherche français ou étrangers, des laboratoires publics ou privés.

1  
2  
3  
4  
5  
6  
7  
8  
9 PETROGENESIS OF MARTIAN SULFIDES IN THE  
10 CHASSIGNY METEORITE

11  
12 JEAN-PIERRE LORAND<sup>1</sup>, SYLVAIN PONT<sup>2</sup>, VINCENT CHEVRIER<sup>3</sup>, AMBRE LUGUET<sup>4</sup>,  
13 BRIGITTE ZANDA,<sup>2</sup> ROGER HEWINS<sup>2</sup>

14 *1 Laboratoire de Planétologie et Géodynamique à Nantes, CNRS UMR 6112,*  
15 *Université de Nantes, 2 Rue de la Houssinière, BP 92208, 44322 Nantes Cédex 3,*  
16 *France. [jean-pierre.lorand@univ-nantes.fr](mailto:jean-pierre.lorand@univ-nantes.fr).*

17  
18 *2 Institut de Minéralogie, de Physique des Matériaux, et de Cosmochimie (IMPMC) - Sorbonne*  
19 *Université- Muséum National d'Histoire Naturelle, UPMC Université Paris 06, UMR CNRS 7590,*  
20 *IRD UMR 206, 61 rue Buffon, 75005 Paris, France.*

21  
22 *3 W.M. Keck Laboratory for Space and Planetary Simulation, Arkansas Center for Space and*  
23 *Planetary Science, MUSE 202, University of Arkansas, Fayetteville, AR 72701, USA.*

24  
25 *4 Rheinische Friedrich-Wilhelms-Universität Bonn, Steinmann Institut für Geologie, Mineralogie*  
26 *und Paläontologie, Poppelsdorfer Schloss, 53115 Bonn, Germany.*

27  
28  
29  
30  
31  
32  
33  
34 Corresponding author: [jean-pierre.lorand@univ-nantes.fr](mailto:jean-pierre.lorand@univ-nantes.fr)  
35  
36

## ABSTRACT

37  
38 The Chassigny meteorite, a Martian dunite, contains trace amounts (0.005 vol.%) of Fe-Ni  
39 sulfides, which were studied from two polished mounts in reflected light microscopy, Scanning  
40 Electron Microscope (SEM) and Electron Microprobe (EMP). The sulfide phases are, by  
41 decreasing order of abundance, nickeliferous (0-3 wt% Ni) pyrrhotite with an average composition  
42  $M_{0.88\pm 0.01}S$  ( $M = Fe+Ni+Co+Cu+Mn$ ), nickeliferous pyrite (0-2.5 wt% Ni), pentlandite, millerite  
43 and unidentified Cu sulfides. Pyrrhotite is enclosed inside silicate melt inclusions in olivine and  
44 disseminated as polyhedral or near spherical blebs in intergranular spaces between cumulus and  
45 postcumulus silicates and oxides. This sulfide is considered to be a solidification product of  
46 magmatic sulfide melt. The pyrrhotite Ni/Fe ratios lie within the range expected for equilibration  
47 with the coexisting olivine at igneous temperatures. Pyrite occurs only as intergranular grains,  
48 heterogeneously distributed between the different pieces of the Chassigny meteorite. Pyrite is  
49 interpreted as a by-product of the low-T (200°C) hydrothermal alteration events on Mars that  
50 deposited Ca sulfates + carbonates well after complete cooling. The shock that ejected the  
51 meteorite from Mars generated post-shock temperatures high (300°C) enough to anneal and  
52 rehomogenize Ni inside pyrrhotite while pyrite blebs were fractured and disrupted into subgrains  
53 by shock metamorphism. The negligible amount of intergranular sulfides and the lack of solitary  
54 sulfide inclusions in cumulus phases (olivine, chromite) indicate that, like other Martian basalts so  
55 far studied for sulfur, the parental melt of Chassigny achieved sulfide-saturation at a late stage of  
56 its crystallization history. Once segregated, the pyrrhotite experienced a late-magmatic oxidation  
57 event that reequilibrated its metal-to-sulfur ratios.

## INTRODUCTION

58  
59  
60  
61 Mars is an S-rich planet (King and McLennan 2010 and references therein). Oxidized  
62 sulfur is a major component of the Martian regolith (up to 8 wt% SO<sub>2</sub>; Foley et al. 2003). Martian  
63 sulfates originated from magmatic degassing of SO<sub>2</sub> (Tian et al. 2015; Kerber et al. 2015), although

64 a minor contribution from acid weathering of pre-existing Fe sulfides is not unlikely (Dehouck et  
65 al. 2012). Owing to their much higher FeO contents, Martian basalts are able to transfer twice as  
66 much S as dissolved FeS from the mantle to the Martian crust compared to terrestrial basalts (Ding  
67 et al. 2015 and references therein).

68 Mars is the only telluric planet of the solar system that can also be studied from meteorites.  
69 More than a hundred igneous rocks ejected from the Martian crust are now available in our  
70 collections and are referred to as SNC meteorites, in addition to a few meteorites containing pieces  
71 of the lithology of the early Martian crust (McSween and Treiman, 1998; Treiman et al., 2000).  
72 SNC meteorites comprise hypovolcanic porphyritic basalts (Shergottites), clinopyroxene cumulates  
73 (Nakhlites) and dunite cumulates (Chassignites) from extrusive flows (McSween 2001; McSween  
74 and McLennan, 2014 and references therein). Studies of shergottites provided invaluable  
75 information on sulfur and sulfides in the interior of Mars. Accessory pyrrhotite was reported as the  
76 predominant Fe-sulfide, coexisting with pentlandite and chalcopyrite (Lorand et al. 2005;  
77 Gattacceca et al. 2013; Franz et al. 2014; Baumgartner et al. 2017a). It is well known that  
78 pyrrhotite phases are oxygen fugacity sensors because trivalent  $\text{Fe}^{3+}$  can balance the charge  
79 deficiency due to the missing  $\text{Fe}^{2+}$  in the pyrrhotite structure (Pratt et al. 1994; Mycroft et al. 1995;  
80 Mikhlin and Tomashevich 2005; Skinner et al. 2004). The range of metal-to-sulfur atomic ratios  
81 ( $0.99 < \text{M/S} < 0.9$  where M = divalent metals Fe, Ni, Co, Cu, Mn) published for shergottite  
82 pyrrhotites is consistent with the range of  $f\text{O}_2$  conditions inferred for the Martian mantle (FMQ +  
83 0.5 to FMQ-3; Herd et al. 2002; Papike et al. 2009; FMQ = Fayalite-Magnetite-Quartz buffer). Fe-  
84 Ni sulfides also are of prime importance for the budget of highly siderophile elements (Platinum-  
85 group elements-PGEs, Au, Re) of Martian magmas, which behave as strongly chalcophile elements  
86 in metal-free magmatic rocks like SNC meteorites (Baumgartner et al. 2017a).

87 The cumulate nakhlites differ from shergottites by their paucity of Fe-Ni sulfides, which are  
88 mainly composed of strongly metal-deficient pyrrhotite phases ( $\text{M/S} = 0.875 \pm 0.01$ ; Chevrier et al.  
89 2011; see also Day et al. 2006). These pyrrhotite compositions are not in equilibrium with the

90 redox conditions inferred for the mantle source of parental melts (Chevrier et al., 2011). Moreover,  
91 hydrothermal alteration products (e.g., pyrite) have been identified in nakhlites (Bunch and Reid,  
92 1975; Greenwood et al. 2000a). The origin of pyrrhotite non-stoichiometry (magmatic degassing,  
93 assimilation of S or post-igneous hydrothermal modification) is still debated (Day et al. 2006;  
94 Chevrier et al. 2011; Franz et al. 2014). Chassignites may provide separate constraints because they  
95 share many characteristics with nakhlites, including their inferred mode of occurrence as extrusive  
96 flow(s) on Mars, their crystallization at ca. 1.3 Ga and their ejection ages at ca. 11 Ma indicating a  
97 single ejection event for chassignites and nakhlites (Harvey and McSween 1992; Treiman et al.  
98 2000; Nyquist et al. 2001; McSween 2001). Chassignites consist of only three meteorites,  
99 Chassigny (Floran et al. 1978; Johnson et al. 1991), northwest Africa (NWA) 2737, a strongly  
100 shocked hot desert find from northwest Africa (Beck et al. 2006) and NWA 8694, a ferroan  
101 chassignite recently discovered from northwest Africa (Hewins et al. 2015). However, chassignites  
102 remain the least well known of the SNC regarding Fe-Ni sulfides, except the highly shocked  
103 sample NWA 2737 that was deeply modified by impact metamorphism (Lorand et al. 2012).

104 Our paper is focused on the Chassigny meteorite that fell on October 3, 1815 in Haute-  
105 Marne, eastern France (Pistollet 1816). It is the oldest fall of a Martian meteorite ever observed on  
106 Earth and, as such, the historical starting point of SNC studies. Shock metamorphism effects in this  
107 meteorite are much weaker than in NWA 2737 (Langenhorst and Greshake, 1999). Unlike  
108 northwest Africa meteorites, it escaped hot desert alteration and the related damage to igneous and  
109 hydrothermal sulfide assemblages (Lorand et al 2005; 2015). Chassigny may allow us to address  
110 the behavior of Fe-Ni sulfides during cooling and hydrothermal circulation in the cumulate parts of  
111 lava flows as well as the timing of S saturation in ferropicritic Martian magmas.

## 113 **PETROGRAPHY OF CHASSIGNY**

114

115 The Chassigny meteorite is a dunitic cumulate composed of cumulus olivine (91.6 vol. %)

116 and chromite (1.4 vol. %), intercumulus pyroxenes (5 vol.%) and feldspar (1.7 vol. %), and  
117 accessory phases (potassium feldspar, apatite, baddeleyite, zirconolite, silica, ilmenite, rutile and Fe  
118 sulfides (Floran et al. 1978; Meyer 2012). The rock microtexture is adcumulate, except where  
119 intercumulus minerals are concentrated (Fig. 1). Olivine is Fe-rich ( $\text{Fo}_{68}$ ). The pyroxenes are Ca-  
120 rich, poikilitic augite ( $\text{Wo}_{33}\text{En}_{49}\text{Fs}_{17}$ ) containing lamellae of exsolved Ca-poor pyroxene  
121 ( $\text{Wo}_3\text{En}_{68}\text{Fs}_{17}$ ) (Johnson *et al.* 1991) and poikilitic pigeonite (Wadhwa and Crozaz 1995).  
122 Interstitial feldspar is Na-rich ( $\text{An}_{32}\text{Ab}_{64}\text{Or}_4$ ). Chassignites are interpreted as cumulates from  
123 ultramafic (ferropicritic) magma(s) emplaced as a komatiitic flow or sill and crystallized at high  
124 oxygen fugacity compared to shergottites ( $\text{FMQ} \pm 1$  log unit vs  $\text{FMQ} + 0.5$  to  $\text{FMQ} -3$  log unit;  
125 Herd et al. 2002; Papike et al. 2009; Delaney and Dyar 2001; Treiman et al. 2007; McCubbin et al.  
126 2013; Baumgartner et al. 2017b). During cooling and solidification, chromite was likely the first  
127 phase to crystallize because it is found as inclusions in olivine, followed by olivine.

128 Olivine encloses large (up to 350  $\mu\text{m}$  across) spherical to elliptical melt inclusions (Floran  
129 et al. 1978; Varela et al. 2000; McCubbin and Nekvasil 2008; Nekvasil et al. 2007; McCubbin et al.  
130 2013). These melt inclusions are interpreted as entrapment of cogenetic melt during magmatic  
131 growth of olivine (McSween and Treiman 1998). Most of these inclusions are partially crystallized  
132 and contain euhedral minerals interpreted as daughter minerals: low-Ca pyroxene (orthopyroxene)  
133 and high-Ca augitic pyroxene together with Cl-apatite and/or Al-rich chromite, magnetite,  
134 kaersutitic amphibole and Ti-biotite (Johnson et al. 1991; Morikawa et al. 2006; McCubbin et al.  
135 2013). These daughter minerals are embedded in a K-Si-Al-rich alkali feldspar glass (alkali  
136 maskelenyite of McCubbin et al., 2013) showing significant Cl (2500-1500 ppm) and  $\text{H}_2\text{O}$  (0.74  
137 wt%) contents (Boctor et al., 2006; McCubbin and Nekvasil 2008).

138 Secondary minerals of Martian origin (trace amounts of Ca-carbonate, Ca-sulfate and Mg-  
139 carbonate) were identified in some cracks inside Chassigny (Wentworth and Goodings 1994).  
140 Sulfates display non mass-dependent  $\Delta^{33}\text{S}$  isotopic compositions deviating from 0 that support a  
141 pre-terrestrial origin for these minerals (Farquhar et al. 2000; Franz et al. 2014).

142

143

## ANALYTICAL METHODS

144

145           The samples in this study consisted of two polished mounts of Chassigny ( $\sim 3 \text{ cm}^2$ ), which  
146 were provided by the Muséum National d'Histoire Naturelle (MNHN), Paris, France. Sulfides were  
147 first characterized with an Olympus BH2 optical microscope operating in reflected light. They  
148 were studied in conventional (high-vacuum) mode with a Tescan VEGA II LSU Scanning Electron  
149 Microscope (SEM) equipped with a silicon drift (Bruker) Energy Dispersive Spectrometer (EDS)  
150 (Muséum National d'Histoire Naturelle-MNHN, Paris, France). Sulfides were localized in the two  
151 samples thanks to mosaics composed of stitched BSE maps with a view field of  $905 \mu\text{m}$  each and  
152 an overlap of 5% (Fig. 1). These maps allowed sulfide modal abundances to be estimated using  
153 their high BSE contrast with non-sulfide minerals (Photoshop<sup>TM</sup> toolbar). The minimum size of  
154 sulfide particle that can be resolved this way was around  $10 \mu\text{m}$ . Then, each sulfide detection was  
155 checked by optical microscopy and EDS spectra collected during manual scan over the two  
156 polished mounts. This procedure helped to take into account the smallest sulfide grains ( $< 5 \times 5$   
157  $\mu\text{m}$ ) not detected on the BSE maps and avoided overestimation of sulfide abundances from  
158 minerals with similar brightness (baddeleyite, ilmenite, chromite).

159           Major element compositions of sulfides were first determined with the SEM-EDS at the  
160 MNHN using 15 keV accelerating voltage with a PhiRoZ EDS standardless procedure and a  
161 working distance of 15.4 mm corresponding to the geometrical configuration of the chamber of the  
162 Tescan VEGA II LSU SEM for semi quantitative analyses. Each grain texture was carefully  
163 studied in BSE mode at high magnification to avoid analytical contribution of silicate  
164 microinclusions or alteration products. The spatial resolution of the SEM (a few hundred  
165 nanometers) allowed tiny contaminants to be resolved and discrete sulfide inclusions inside  
166 olivine-hosted melt inclusions to be analyzed semi quantitatively. Contaminants, however small,  
167 were monitored by analyzing silica and phosphorus which are major elements in the minerals



194 Five sulfide phases were identified in our polished mounts of Chassigny. These are by  
195 decreasing order of abundance: pyrrhotite, pyrite, pentlandite, Cu-sulfides and millerite. Sulfides  
196 occur as both enclosed and intergranular sulfides.

### 197 **Enclosed sulfides**

198 The sulfides do not occur as solitary sulfide blebs in cumulus minerals (olivine and  
199 chromite). Enclosed sulfides occur exclusively inside melt inclusions in olivine (Fig. 2a). Olivine-  
200 hosted enclosed sulfides are a pyrrhotite phase of very small size (1 x 1 to 5 x 3  $\mu\text{m}$ ). Pyrrhotite  
201 may occur as prismatic crystals with hexagonal cross sections that may occasionally be ragged on  
202 one face (Fig. 2a). The pyrrhotite is commonly associated with chromite, apatite, orthopyroxene,  
203 clinopyroxene and kaersutite, which represent crystallization products from the melt fraction  
204 trapped inside the melt inclusions (McCubbin and Nekvasil 2008). The sulfide grain usually occurs  
205 close to the inner walls of the cavity; it may also be occasionally located within polycrystalline  
206 aggregates of pyroxenes, chromite and apatite.

### 207 **Intergranular sulfides**

208 Intergranular sulfides range in size from less than 100  $\mu\text{m}^2$  to 600  $\mu\text{m}^2$  for the largest ones  
209 (30  $\mu\text{m}$  x 20  $\mu\text{m}$ )(Fig. 3). Their surface area represents less than 0.005 vol. % of the total surface  
210 investigated in this study. Intergranular sulfides are randomly scattered throughout our two  
211 polished mounts of Chassigny (Fig. 1). They fill space at boundaries between olivine grains as well  
212 as triple junctions between olivine and pyroxenes, or olivine and chromite. Some intergranular  
213 sulfides are partly embedded inside intergranular feldsparic melt pockets (Fig. 2b). The shape of  
214 intergranular sulfides depends on their location in the meteorite. Sulfide grains embedded in  
215 feldsparic melt pockets may preserve rounded morphologies (Fig. 2c). Intergranular sulfide may  
216 show straight contacts against olivine crystals (Fig. 2d). Those grains located at triple junctions  
217 between cumulus minerals (olivine, chromite) or intercumulus pyroxenes are ellipsoidal to  
218 polyhedral bodies with convex-inward grain boundaries and low dihedral angles (Fig. 2e).

219 Intergranular sulfides consist of either predominant pyrrhotite or pyrite. Pyrrhotite exhibits

220 a strong optical anisotropy in reflected light while the pyrite is isotropic, enabling easy distinction  
221 with marcasite. Pyrrhotite and pyrite are randomly distributed throughout the two polished mounts  
222 investigated. Pyrrhotite is predominant in one polished mount while pyrite is for the second one.  
223 Pyrrhotite and pyrite have been found to coexist in a handful of single grains. In that case, a pyrite  
224 rim is observed around the pyrrhotite and the interface between the two phases is corrugated.

225 Pyrrhotite grains are either optically homogeneous or cut by contorted fracture planes (Fig.  
226 2c-e). However, pyrrhotite is slightly fractured compared with major silicates, chromite, and pyrite  
227 (see below). Pentlandite was identified with its optical properties in reflected light (Fig. 2d) and  
228 EDS spectra in five pyrrhotite blebs over the several tens studied in detail with the SEM. In those  
229 grains pentlandite is concentrated as tiny discrete bodies toward the margins of their host pyrrhotite  
230 (granule exsolution, Fig. 2d,e). Copper was detected in two EDS spectra of pyrrhotite/pentlandite  
231 and pyrite suggesting that Cu-sulfides too small to be accurately identified may also be present in  
232 Chassigny intergranular sulfides. One pyrite bleb encloses a Ni-rich sulfide (millerite-NiS) which  
233 was identified with the SEM (Table 2).

234 Euhedral pyrite crystals have not been observed. Intergranular pyrite grains show the same  
235 size and morphologies as pyrrhotite grains: rounded to ellipsoidal bodies or polyhedral grains with  
236 low dihedral angles when forming triple junctions with surrounding olivine (Fig. 2f-h). On average,  
237 pyrite appears to be more fractured compared to pyrrhotite. Fracture networks are evenly  
238 distributed, ranging from a few parallel cracks to regularly spaced cell-like systems; in most  
239 extreme cases, pyrite crystals were fragmented into particles of less than 1-2 micrometres across  
240 (Fig. 2f-h). Fracture planes are generally confined to the pyrite alone (i.e., they do not cut across  
241 surrounding silicates). Pyrite shows incipient alteration by Fe-oxyhydroxides that selectively  
242 replace pyrite along its fracture planes (Fig. 2h).

243

244

## PHASE CHEMISTRY

245 Only a few olivine-hosted pyrrhotite microinclusions were large enough for EMP analysis.

246 Their metal-to-sulfur atomic ratio ranges from 0.86 to 0.90 (Fig. 4; Table 2). These compositions  
247 correspond to hexagonal ((Fe,Ni)<sub>9</sub>S<sub>10</sub>) and monoclinic ((Fe,Ni)<sub>7</sub>S<sub>8</sub>) crystal structures in the low-  
248 temperature phase diagram of natural pyrrhotites (Kissin and Scott, 1982). Nickel concentrations  
249 vary between 1.3 and 2.8 wt% (Fig. 5).

250 Intergranular pyrrhotite exhibits very similar compositions to those of enclosed pyrrhotite  
251 (Fig. 4). EDS and WDS analyses provided reproducible results, as long as the grains analyzed were  
252 more than 10 μm across and devoid of any pentlandite exsolutions (Table 2 and Table S1). The  
253 M/S of intergranular pyrrhotites spread over a restricted range (0.87 - 0.92), with an average  
254 centered on 0.88 ± 0.01 (one standard deviation). The lowest ratio corresponds to intergranular  
255 pyrrhotite showing incipient crystallization of pyrite. The highest ratios (>0.9) were found in the  
256 pyrrhotite grains showing pentlandite micro-exsolution (e.g., Po1a16; Table 2) and/or Cu-rich areas  
257 (e.g., Po7c10; Table 2). These metal-rich pyrrhotite compositions were probably contaminated by  
258 pentlandite exsolutions. Nickel concentrations range between 1 and 3 wt% Ni, irrespective of the  
259 M/S ratios and the occurrence of pentlandite (Fig. 5). The highest Ni contents (>2 wt%) were found  
260 in interstitial pyrrhotite grains located between cumulus olivine crystals. Cobalt contents are below  
261 limits of detection (<0.2 wt%) as are Cr contents except in the vicinity of chromite. Pyrrhotite is  
262 also poor in oxygen (< 1 wt%; Fig. 6).

263 The few EDS analyses of pentlandite correspond to Fe-rich compositions (Table 2), as  
264 expected for this sulfide when it is associated with pyrrhotite (Misra and Fleet, 1973).

265 Pyrite is slightly metal enriched compared to stoichiometric FeS<sub>2</sub> (Fe/S atomic ratio = 0.50-  
266 0.54; Fig. 6). EDS and EMP analyses show heterogeneous distribution of Ni, without any well-  
267 defined Ni-rich spots as reported in NWA 7533 euhedral pyrite grains (Lorand et al. 2015). On  
268 average, pyrite is depleted in Ni compared to pyrrhotite (<0.1-1 wt%; Fig. 5). Its Co content is  
269 below limits of detection for most analyses (Table 2). Among other minor and trace elements,  
270 pyrite contains copper (up to 0.23 wt%) and some oxygen. High oxygen contents (3.4 wt%)  
271 correlate with high M/S ratios thus indicating decreasing S content at increasing oxygen content

272 (Fig. 6).

273

274

## DISCUSSION

275

276

277

278

279

280

281

282

283

284

285

286

287

288

289

290

291

292

The sulfide phases documented here were previously reported by Floran et al. (1978) and Greenwood et al (2000b). The olivine-hosted sulfides and intergranular sulfides define two sulfide assemblages I) pyrrhotite ( $\pm$  pentlandite  $\pm$  Cu sulfides), II) pyrite ( $\pm$  millerite  $\pm$  Cu-sulfides). Assemblage I is typical of SNC igneous meteorites either as intergranular assemblages (Lorand et al. 2005; Chevrier et al. 2011; Franz et al. 2014) or as olivine-hosted sulfides reported in Iherzolitic and picritic (olivine-rich) shergottites (Gattacceca et al. 2013; Baumgartner et al. 2017a). The igneous origin of assemblage I in the Chassigny meteorite is supported by its occurrence in olivine-hosted melt inclusions and the shape of intergranular pyrrhotite grains ranging from nearly spherical droplets to polyhedral grains with concave-inward margins. By its compositions and its shape, assemblage I can be interpreted as a solidification product of magmatic sulfide melts (e.g. Naldrett et al. 1967; Craig and Kullerud 1969; Raghavan 2004; Naldrett 2005 and references therein). By contrast, pyrite is a post-igneous replacement product of the original magmatic sulfide assemblage on Mars because it occurs only as an intergranular, heterogeneously distributed mineral in the intercumulus spaces, while showing similar crystalline shape as pyrrhotite. Before further discussion of their origin, it is necessary to assess the effect of shock metamorphism and post-shock alteration that affected both sulfide assemblages.

### **Shock effect and terrestrial alteration.**

293

294

295

296

297

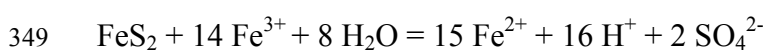
Both pyrrhotite and pyrite are fractured, especially the pyrite. Fracture affects all minerals in the Chassigny meteorite, silicates, phosphates, oxides and sulfides. Olivine-hosted melt inclusions are surrounded by radial fracture planes which may reach intergranular pores of the rock. These fracture networks are usually ascribed to the shock event that launched the meteorite into space, ca 11 Myr ago (Langenhorst and Greysake 1999, Malavergne et al. 2002; Meyer 2012

298 and references therein). However, pyrite displays a much higher density of fracture, resulting  
299 locally in finely granulated pyrite blebs (Fig. 2h). Pyrite behaves as an extremely brittle mineral  
300 resulting in cataclastic deformation during deformation and metamorphism (McClay and Ellis  
301 1983). One may note that at temperatures up to 400°C and confining pressures up to 1000 MPa,  
302 pyrite strain rates range from  $10^{-4}$  to  $10^{-7}$  sec<sup>-1</sup> (McClay and Ellis 1983 and ref. therein). Generally,  
303 the brittle deformation results in randomly fractured fragments (cataclastic texture), as documented  
304 in Chassigny pyrite (Fig. 2g,h). Pyrrhotite behaves more plastically and recrystallizes easily (Cox  
305 1987). Langenhorst and Greshake (1999) studied in detail the shock metamorphism features of the  
306 Chassigny meteorite by optical and transmission electron microscopy (TEM). These authors  
307 documented i)-the activation of numerous planar fractures and dislocations in olivines coexisting  
308 with discontinuous fractures, strong mosaicism and clino-/orthoenstatite inversion, ii)-fracturing,  
309 reduced birefringence (conversion to diaplectic glass (maskelynite), and planar deformation  
310 features in the plagioclase. Taken altogether, these shock features indicate a shock pressure of  
311 about 35 Gpa with a post-shock temperature of about 300°C (Malavergne et al. 2002) without the  
312 impact melting found in other Martian meteorites. The post shock temperature of 300°C proposed  
313 for Chassigny was too low to remelt pyrite which is a stable phase below 743°C under P-T  
314 conditions of planetary surfaces (Toulmin and Barton, 1964). However it was high enough to  
315 anneal and rehomogenize any pentlandite exsolution inside the pyrrhotite: at this temperature, the  
316 Chassigny pyrrhotite compositions plot in the single-phase domain corresponding to monosulfide  
317 solid solution (Mss), the high-temperature precursor of pyrrhotite and pentlandite in the Fe-Ni-S  
318 ternary diagram of Fig. 7. It may be deduced from Fig. 7 that the few pentlandite blebs observed in  
319 Chassigny pyrrhotite exsolved during post-shock cooling by heterogeneous nucleation (Etschman  
320 et al. 2004).

321 The persistence of pyrite and metal-deficient pyrrhotite in the Chassigny meteorite is  
322 consistent with a much lower post-shock temperature and weaker shock effect compared to NWA  
323 2737. Bogard and Garrison (2008) suggested that NWA 2737 experienced a post-shock

324 temperature to 300–500 C, perhaps 800 C. i.e. closer to the upper thermal stability of pyrite.  
325 Indeed, Lorand et al. (2012) reported for this meteorite, minute amounts (0.01 vol.%) of a pyrite-  
326 free, metal-saturated Fe-Ni sulfide assemblage consisting of a Ni-poor troilite (FeS, sometimes Cr-  
327 bearing) coexisting with micrometer-sized native Ni-Fe alloys, in addition to a few Os-Ir alloys.  
328 Lorand et al. (2012) proposed that the high shock pressure (55 Gpa) coupled with strong heating  
329 triggered sulfur degassing that reduced pyrite and metal-deficient pyrrhotite into FeS and native  
330 metal alloys. This shock-induced S loss is supported by the highly resorbed and denticulated shape  
331 of sulfide blebs and their spongy textures (Lorand et al., 2012). An FeS phase was reported to  
332 occur locally in the Chassigny meteorite by Floran et al. (1978). Chevrier et al. (2011) interpreted  
333 this phase as an analytical artifact in the EMP analyses of pyrrhotite. However, as shown by the  
334 sulfide assemblage of NWA 2737, it may have been produced by local S loss during shock  
335 metamorphism. Gattaceca et al. (2013) reported similar evolution of pyrrhotite compositions  
336 toward FeS in the highly shocked olivine-phyric shergottite Tissint. If present, this stoichiometric  
337 FeS phase is likely a very minor phase in the Chassigny meteorite. We did not identify it in our two  
338 polished mounts (Fig. 4). Franz et al. (2014) did not detect the Acid Volatile Sulfides (AVS)  
339 fraction that would correspond to this FeS phase in their chemical extraction of sulfur from  
340 Chassigny.

341 Pyrite has been oxidized after crystallization as shown by its elevated (though variable)  
342 oxygen contents detected by EMP analyses and local replacement by Fe oxyhydroxides. The latter  
343 alteration of pyrite by Fe oxyhydroxides is a typical feature of weathering that releases S as soluble  
344 sulfate while leaving insoluble trivalent Fe as Fe oxyhydroxides (Wattmuff 1974; Thornber 1975;  
345 Lorand et al. 2005; Zurfluh et al. 2013; Hayes et al. 2014). In humid and aerated conditions, pyrite  
346 can be oxidized by oxygen or trivalent Fe following the reactions below (Jerz and Rimstidt 2004;  
347 Liu et al. 2009; Huminicky et al. 2009) :



350 This alteration event is likely a terrestrial feature because Fe oxyhydroxides were observed to occur  
351 only within the finely granulated pyrite blebs showing cataclastic microtextures (Fig. 2h).  
352 However, the Chassigny meteorite is an observed fall and not a hot desert find: its pieces were  
353 collected immediately after their arrival on the Earth surface (Pistollet, 1816), which certainly  
354 prevented them from extensive weathering by atmospheric agents (Meyer, 2012). However,  
355 oxidation may have occurred during the curation of the meteorite for the last 200 years in the  
356 MNHN collection. It is well known from museum curators and mining operation that pyrite can  
357 alter over days or months if kept in a humid and oxygenated environment (Huminicky et al. 2009).  
358 There is independent evidence of terrestrial contamination and/or alteration involving water, sulfur  
359 and sulfides in the Chassigny meteorite. Wentworth and Gooding (1994) reported traces of  
360 massive, fine-grained Ca-sulphate in some vugs in Chassigny's fusion crust which could indicate  
361 either terrestrial contamination or post-fall leaching of hygroscopic, pre-terrestrial salts from the  
362 interior. Terrestrial hydrogen exchange was documented by Leshin et al. (1996) via D/H ratios.  
363 Brandon et al. (2000) documented disturbance in the bulk-rock  $^{187}\text{Re}/^{188}\text{Os}$  ratio of Chassigny  
364 possibly due to late terrestrial remobilization of Re liberated from altered pyrite.

365         The sensitivity of Chassigny pyrite to oxidation can be ascribed to the extensive fracturing  
366 that generated highly granulated domains inside pyrite grains. In impact regolith breccia NWA  
367 7533, terrestrial weathering was guided by shock-induced microfracturing of pyrite (Lorand et al.  
368 2015). The size of the pyrite grains plays a key part in the oxidation process which destroys  
369 museum samples of pyrite and marcasite (Rimstidt and Vaughan 2003). It is well known that  
370 milling and grain size reduction increases the rate and susceptibility of Fe-bearing phases to  
371 oxidation processes (Williamson and Rimstidt 1994; Pratt et al. 1994; Nesbitt et al. 1998; Thomas  
372 et al. 1998, 2001). Conchoidal fractures that produce surface sites of reduced coordination with  
373 dangling bonds are more reactive compared to normal crystallographic surfaces sites (Chandra and  
374 Gerson 2011; Todd et al. 2003). Compared with pyrite, Chassigny pyrrhotite shows almost  
375 unaltered, oxygen-poor compositions which are at odds with theoretical expectations. Pyrrhotite is

376 expected to be far more reactive to oxidation than pyrite (Janzen et al. 2000; Mikhlin and  
377 Tomashevich 2005). The weathering of pyrrhotite under the influence of atmospheric oxygen  
378 proceeds approximately 20–100 times faster than that of pyrite (Belzile et al. 2004). This faster  
379 oxidation rate is usually ascribed to the lower crystal symmetry of pyrrhotite that results from the  
380 vacancy of Fe atoms in the crystal structure (Janzen et al. 2000, Harries et al. 2013). Concerning  
381 Chassigny pyrrhotite, its very low degree of alteration could be due to extensive recrystallization  
382 at 300°C during the shock metamorphism event that probably healed fracture planes, thus reducing  
383 preferential pathways for oxidation.

384

### 385 **Martian hydrothermal alteration and the origin of pyrite.**

386 By its location in interstitial pores, pyrite clearly postdates solidification of the cumulate  
387 phases of the Chassigny meteorite. Crystallization of pyrite at the igneous stage is very unlikely as  
388 it is not stable above 743°C (Toulmin and Barton 1964). Moreover, its precipitation at this  
389 temperature would require unrealistically high sulfur fugacity (close to the domain of liquid native  
390 S) compared with that indicated by pyrrhotite composition (Fig. 8). Both lines of evidence make  
391 pyrite a subsolidus phase. Pyrite can exsolve from pyrrhotite by cooling but exsolution should  
392 produce Py inside Po, as wormlike textures (e.g., Lorand and Alard 2011) or discrete granules as  
393 usually observed in magmatic sulfide assemblages (Craig and Vokes 1993; Hall 1986; Hollwell et  
394 al. 2017 and references therein). Precursor high-temperature monosulfide solid solution (Mss) can  
395 produce only 30% pyrite by weight this way (Naldrett et al. 1967). Assuming that pyrite exsolved  
396 from metal-deficient pyrrhotite with a general composition of  $M_{0.88}S$ , the exsolution process should  
397 have followed path B in Fig. 8 on cooling; hence the pyrrhotite should display increasing metal-to-  
398 sulfur ratio down to 0.92 at  $T < 200^\circ\text{C}$ , significantly off the compositional range measured for the  
399 Chassigny meteorite (Fig. 4). If exsolved from the pyrrhotite, then pyrite should be homogeneously  
400 distributed within our two polished mounts of Chassigny, and observed both as inclusions and  
401 intergranular sulfides.

402 The shape of pyrite grains that display the same morphologies as coexisting igneous  
403 pyrrhotite grains argues instead for local replacement of the pyrrhotite by pyrite. The same  
404 replacement reaction was postulated for pyrite from other Martian meteorites (e.g. ALH 84001;  
405 Shearer et al. 1996; the nahklites Nakhla, Governador Valadares and Lafayette; Bunch and Reid  
406 1975; Greenwood et al. 2000a; Franz et al. 2014). In the  $\log f_{S_2}$ -T diagram of Fig 8, single-phase  
407 pyrite grains observed in Chassigny reflect local excursion of the fugacity of sulfur within the  
408  $\log f_{S_2}$ -T area of pyrite stability, i.e. well above the FMQ-Po reference curve taken as a marker of  
409 redox conditions for Chassigny. This cooling path may track input of external S raising the  
410 apparent fugacity of sulfur (Hall 1986). There is published evidence for post-igneous external input  
411 of S in the Chassigny meteorite. Wentworth and Gooding (1994) reported discontinuous veins of  
412 Ca-sulphate (gypsum ( $CaSO_4 \cdot 2H_2O$ ) or bassanite ( $CaSO_4 \cdot \frac{1}{2}H_2O$ )), Ca-carbonate, and Mg-  
413 carbonate along fractures in primary igneous minerals. These sulfate and carbonate salts also  
414 contain traces of Cl and P, which supports their precipitation from short-lived, cold, saline, aqueous  
415 solutions well after the igneous crystallization of the Chassigny cumulate (Bridges et al., 2001).  
416 Sulfur isotopic compositions measured on the Chassigny meteorite add further constrains on the  
417 origin of pyrite. Greenwood et al (2000b) provided seven *in-situ* ion microprobe analyses of this  
418 sulfide; all show negative Canyon Diablo Troilite (CDT)-normalized  $\delta^{34}S$  ( $-4.6\text{‰} < \delta^{34}S < -1.5\text{‰}$ ),  
419 off the baselines for mantle-derived Martian sulfur ( $\delta^{34}S = 0$ ) as defined from shergottite meteorites  
420 (Franz et al. 2014). Greenwood et al (2000b) inferred low-temperature (200°C) exchange of  
421 volatile components (S, C, H) between olivine cumulate flows and regolith by hydrothermal fluids.  
422 Likewise, Franz et al. (2014) documented mass-independent fractionation (MIF) in Chassigny Ca  
423 sulphates ( $\Delta^{33}S = 0.0336 \pm 0.008 \text{‰}$ ) which also indicates recycling of surface sulfur.

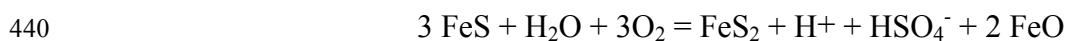
424 Chassigny pyrite may have formed from direct sulfurization of preexisting igneous  
425 pyrrhotite by S-bearing hydrothermal fluids because the latter imparted their S isotopic  
426 composition to the pyrite, different from that of initial igneous sulfides. Different pathways can be  
427 assumed for this transformation, depending on the initial assemblage of the igneous sulfide and

428 chemical exchanges between sulfides and hydrothermal fluid. For example, the NiS-rich mineral  
429 identified as millerite with the SEM in one pyrite grain could derive from a pyrrhotite-pentlandite  
430 precursor, if this reaction also operated with Fe loss to the fluid (Fig. 9). Pyrite and millerite are  
431 stable together below 230°C (Craig 1973; Misra and Fleet 1973), in agreement with the  
432 temperature range inferred for hydrothermal contamination of the Chassigny meteorite  
433 (Greenwood et al., 2000b). A volume loss of several tens percent of original sulfides is expected  
434 for this reaction (e.g. Holwell et al. 2017, and ref. therein) but hard to quantify as the Chassigny  
435 sulfides experienced shock effects that heavily fractured the pyrite and modified its porosity.

436 There are other possible pathways for pyrite formation in the Chassigny meteorite.  
437 Pyrrhotite can be oxidized into pyrite via reactions such as:



439 or



441 in humid and aerated conditions (Watmuff 1974; Pratt et al. 1994; Harries et al. 2013;  
442 Kanipayacharoen and Boudreau 2013). However, such reactions are considered to be much less  
443 likely because the Chassigny cumulate flow was exposed to subsurface conditions of dry  
444 Amazonian Mars (Nyquist et al., 2001), a period of little water and dissolved oxygen available for  
445 oxidative dissolution of pyrrhotite.

446 Our study, coupled with literature data, reveal strong heterogeneity in the distribution of  
447 pyrite both within and between each piece of the same meteorite. The pyrite/pyrrhotite modal ratio  
448 is estimated to vary from ca 1 to 2 between our two polished mounts. Greenwood et al (2000b)  
449 identified only pyrite in a sulfide-poor chip of Chassigny. This heterogeneity is an expected  
450 outcome of the numerous parameters that drive pyrite-producing reactions. For instance, pyrrhotite  
451 armored inside olivine-hosted sulfide inclusions escaped to alteration while unarmored portions  
452 within intercumulus material have been heterogeneously replaced. One may also argue that pyrite  
453 did not systematically nucleate because its formation is very sluggish below 200° C (Craig, 1973;

454 Rickard and Luther 2007 and references therein). Additional evidence of internal heterogeneity is  
455 the heterogeneous distribution of marcasite. Floran et al. (1978) identified this sulfide, based only  
456 on its optical properties, while we did not find it in our polished mounts of Chassigny. Marcasite  
457 was reported to form at  $T < 150^{\circ}\text{C}$  and  $\text{pH} < 4$  by Fleet (1978) and Craig and Vokes (1993 and  
458 references therein). One may argue that the post-shock annealing event at  $300^{\circ}\text{C}$  converted  
459 marcasite to pyrite. On Earth, for example, marcasite in sulfide ore deposits is converted to pyrite  
460 by natural annealing at relatively low ( $< 200^{\circ}\text{C}$ ) temperatures (Fleet 1978; Hall 1986; Murowchick,  
461 1992). The heterogeneous distribution of marcasite may thus fingerprint some heterogeneities in  
462 the Chassigny meteorite related to shock metamorphism, as do the occasional occurrences of FeS  
463 (troilite).

464

#### 465 **Petrogenesis of the igneous sulfide assemblage I.**

##### 466 **Sulfur ultradepletion in Chassigny indicates sulfur-undersaturated parental melt.**

467 The lack of single-phase pyrrhotite inclusions indicates that the parental melt for the  
468 Chassigny meteorite presumably did not segregate immiscible sulfide liquids over the interval of  
469 olivine and chromite crystallization. Sulfur dissolves in reduced Martian basalts as  $\text{FeO} + 1/2\text{S}_2 =$   
470  $\text{FeS} + 1/2\text{O}_2$  (Ding et al., 2015 and references therein). The S content necessary to saturate the  
471 hypothetical parental melt of Chassigny is available from experiments relevant to Martian lavas  
472 (Ding et al. 2015), coupled with the FeOT content (19.95 - 20.33 wt%; Johnson et al. 1991;  
473 Filiberto 2008; He et al. 2013). Giesting et al. (2015) estimated that partial melting started at  $P > 2$   
474 Gpa (170 km) so this putative melt was able to dissolve at best  $4000 \pm 1000$  ppm S (Ding et al.  
475 2015). Its actual S content can be estimated around 3600 ppm by coupling the most conservative  
476 estimate of the S content of the Martian mantle ( $360 \pm 120$  ppm S; Wang and Becker 2017) with  
477 the degree of partial melting estimated for Chassignites (10%; Wadhwa and Crozaz 1995). Of  
478 course, melting degrees in excess of 10% would have decreased the S content of the melt  
479 proportionally, thus making it S-undersaturated once leaving its mantle source. Our conclusion is

480 supported by platinum-group element (PGEs) analyses. Baumgartner et al (2017b) reported  
481 detectable concentrations of Ru (up to ~160 ppb Ru) in chromite of Chassigny and NWA 2737.  
482 This element (and other PGEs as well) should have been preferentially incorporated into sulfide  
483 melts if any sulfide had been present during chromite precipitation (Brenan et al., 2016 and  
484 references therein). Baumgartner et al (2017b) concluded that the parental melt of Chassigny  
485 started crystallizing chromite under sulfide-undersaturated conditions, as documented for other  
486 Martian magmas sampled by shergottites (e.g. Brandon et al. 2012; Baumgartner et al. 2017a).

487         The late-magmatic achievement of S saturation is also consistent with the very low amount  
488 of Fe-Ni sulfides in the Chassigny meteorite. Previous studies reported bulk-rock S contents of  
489 similar order of magnitude in Chassigny (mean  $260 \pm 130$  ppm S; McSween, 2014) and nakhlites,  
490 corresponding to ca.,  $0.06 \pm 0.03$  wt% Fe-Ni sulfides composed of 50% pyrite and 50% pyrrhotite.  
491 By contrast, our two polished mounts are depleted in Fe-Ni sulfides by a factor 10 (Table 4). The  
492 same depletion was also reported by Franz et al. (2014) who concluded that over 99% of the sulfur  
493 recovered by their chemical extraction from Chassigny ( $65 \pm 1$  ppm) correspond to Ca-sulphates,  
494 while a negligible fraction ( $< 3$  ppm) correspond to sulfides (pyrite and metal-deficient pyrrhotite,  
495 i.e. Chrome Reduced Sulfide, CRS). The bulk-rock Ni budget also reflects the negligible volume of  
496 Fe-Ni sulfides in Chassigny. Olivine alone is able to balance the bulk rock Ni contents ( $500 \pm 70$   
497 ppm; Papike et al. 2009) if we combine our analyses of olivine in Table 3 ( $530 \pm 30$  ppm Ni) with  
498 the olivine modal proportions reported in the literature (91%; Meyer, 2012). By contrast, the  
499 contribution of Fe-Ni sulfides is at best 1-2 ppm (within the analytical error of the bulk-rock Ni  
500 content) for the maximum Ni concentration of 3 wt% in the sulfides and a modal volume of 0.005  
501 % (Fig. 7).

502         The amount of sulfide precipitated in Chassigny is negligible compared to the expected  
503 huge amount of S the parental melt was able to dissolve. Because Fe-Ni sulfides preferentially  
504 segregated in the intercumulus pores of the meteorite, their amount primarily reflects the low  
505 amount of trapped intercumulus silicate melt. Other parameters may also have contributed in

506 producing negligible amount of sulfides, i-an unrealistically high degree of partial melting  
507 compared to the accepted values, ii-second stage melting of a S-depleted, LREE-depleted olivine-  
508 augite mantle source, iii-late-stage migration/removal of intergranular sulfides by percolating  
509 fluid(s), iv- S outgassing or sulfide resorption driven by late-stage melt decompression that was  
510 coeval with the extrusion of the Chassignite cumulate pile to near-surface conditions. Any further  
511 discussion of these parameters will require detailed in-situ geochemical studies of trace metals in  
512 Fe-Ni sulfides, which were hitherto made impossible by the very small size of these sulfides  
513 (Baumgartner et al., 2017a,b).

514

### 515 **In-situ nucleation of Ni-pyrrhotite**

516 Models based on previously published S contents of Chassigny ( $260 \pm 130$  ppm S)  
517 suggested that Chassigny Fe-Ni sulfides originated from mixing between cumulates from S-  
518 undersaturated melts with S-saturated melts or externally derived evolved melt (see Ding et al.  
519 2015, Baumgartner et al 2017b). The new bulk-rock S estimates (Franz et al. 2014) and our own  
520 observations make such interpretations disputable. In-situ nucleation of sulfides from the trapped  
521 intercumulus melt is more likely, especially by considering sulfides from olivine-hosted melt  
522 inclusions. Such enclosed sulfides resemble early solid micro - precipitate growth in a fluid  
523 medium. One may surmise that sulfides appeared very early in these inclusions because the trapped  
524 silicate melt fractions were strongly FeO-depleted after massive precipitation of olivine; olivine  
525 melt inclusions started crystallizing at high pressure, under conditions of lowered S saturation  
526 according to experiments on terrestrial (e.g. Mavrogenes and O'Neill, 1999) and martian basalts  
527 (Ding et al., 2015). Pressure above 0.4 Gpa to as high as 2 Gpa were suggested by Nekvasil et al.  
528 (2007, 2009), Filiberto (2008) and Giesting (2015). McCubbin et al. (2008) estimated  $P = 0.9$  Gpa  
529 from the crystallization path of Chassigny melt inclusions that contain 0.48–0.67 wt% H<sub>2</sub>O (He et  
530 al. 2013). These high water contents, coupled with high alkali contents, delayed full solidification  
531 of olivine-hosted melt inclusions down to  $T = 700^{\circ}\text{C}$  (McCubbin et al. 2013). Enclosed pyrrhotites  
532 in theory have a solidification temperature of ca.  $1200^{\circ}\text{C}$  at 1 bar (Craig and Kullerud, 1969 and

533 references therein) that accounts for their segregation as euhedral solid crystals along with apatite  
534 and low-Ca pyroxene.

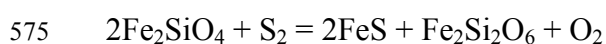
535         The shape of intergranular assemblages, i.e. ovoid grains or triangular-shaped grains  
536 showing convex-inward margins and low dihedral angles with matrix silicates are characteristic of  
537 immiscible sulfide blebs forming isolated pockets in cumulate rocks (Naldrett 2005 and references  
538 therein). Textural reequilibration that typically affects sulfides in cumulate igneous rocks is  
539 recognized through straight triple junctions with olivine and chromite meeting at 120° indicating  
540 surface energy minimization between solids. According to Giesting et al (2015), after accumulation  
541 of olivine at  $T = 1230^{\circ}\text{C}$  and 0.9-1.7 Gpa, the putative lava flow was decompressed from 1 to 0.02  
542 Gpa and cooled rapidly from a point where temperatures were 800–850 °C at a depth of no more  
543 than ~200 m (Treiman et al. 2007; McCubbin et al. 2013). The interstitial magma that cooled to  
544 form the mesostasis of olivine cumulates experienced retrograde boiling and degassing of volatiles,  
545 especially H<sub>2</sub>O (McCubbin and Nekvasil 2008; McCubbin et al. 2013; Giesting et al., 2015). This  
546 degassing also triggered complete solidification of the mesostasis at higher  $T$  (>900°C) compared  
547 to melt inclusions in olivine, thus preventing sulfide melts from migrating through the cumulate  
548 pile. Chemical equilibrium between sulfides and olivine can be tested with the partitioning  
549 behavior of Ni. Despite between-grain variations of Ni/Fe on a localized scale, the mean partition  
550 coefficient  $K_d$  (Ni/Fe sulfides/Ni/Fe olivine) calculated from our olivine and pyrrhotite  
551 compositions (Fo 68, 0.06 wt% NiO for olivine, Table 3 and supplementary data;  $2 \pm 0.5$  wt% Ni  
552 for pyrrhotite) is in good agreement with the experimental values determined at magmatic  
553 temperatures ( $19 \pm 5$  vs. 13 to 15; Brenan, 2003). Thus, an overall state of equilibrium seems to  
554 have existed between intergranular (and enclosed) Chassigny pyrrhotite and coexisting olivine as  
555 regard the Ni-Fe partitioning. This is expected where sulfides segregated in-situ.

556

### 557         **Pyrrhotite compositions track late-magmatic oxidation-crustal contamination**

558         Our data show that a metal-deficient pyrrhotite composition of general formula  $M_{0.88}\text{S}$  (M

559 = Fe + Ni + Co + Cu + Mn) is the main igneous sulfide in the Chassigny meteorite. It has long been  
560 suggested that disseminated sulfides in volumetrically dominant silicate rocks reequilibrate through  
561 redox equilibrium involving coexisting silicate assemblages (Barton 1970). The Chassigny  
562 pyrrhotite compositions cluster within a narrow  $\log f_{S_2}$ -T domain of Fig. 8, well above the  
563 reference buffer curve Fayalite-Magnetite-Quartz-Pyrrhotite (FMQ-Po) at solidus temperature. The  
564 accepted magmatic  $f_{O_2}$  conditions for Chassigny are slightly below FMQ (FMQ-1.25 log units;  
565 McCubbin et al 2013), whether calculated with the equilibrium olivine + low-Ca pyroxene + Cr-  
566 spinel (Treiman et al. 2007) or from V valence-state oxybarometer (Baumgartner et al. 2017b; see  
567 also Beck et al. 2006). For such  $f_{O_2}$  conditions, the igneous pyrrhotite compositions should be  
568 more metal-rich ( $M_{0.96}S$ ) at magmatic temperatures compared to the measured composition (Fig.8).  
569 Of course, the latter may not be representative of the high temperature pyrrhotite composition  
570 because of subsolidus reequilibration. A cooling path following the FMQ-Po reference buffer curve  
571 can lower pyrrhotite M/S ratios down to at best 0.91 before pyrite starts exsolving at ca 250°C  
572 (path A; Fig. 8). Nevertheless, the latter value still excludes almost all the measured pyrrhotite  
573 compositions. The fugacity of oxygen necessary to reproduce the composition of the Chassigny  
574 pyrrhotite can be estimated from the sulfidation reaction of olivine



576 Eggler and Lorand (1993) calibrated this equilibrium as a barometer for oxygen and sulfur  
577 fugacity. The fugacity of S is deduced from the FeS isopleths in Fig. 8. Using the compositions of  
578 olivine and low-Ca opx in Chassigny (Fa<sub>32</sub> and En<sub>70</sub>; Meyer, 2012 and Table 3), the sulfidation  
579 reaction of olivine indicates an  $f_{O_2}$  value close to FMQ + 2 log units at 800-900°C (equation 46 in  
580 Eggler and Lorand 1993). Such conditions are significantly more oxidizing compared to the  $f_{O_2}$   
581 range deduced from Cr spinel compositions (McCubbin et al., 2013; Baumgartner et al. 2017b).

582 The same discrepancy between expected and measured pyrrhotite compositions was  
583 documented for nakhlites (Chevrier et al. 2011). Indeed, in addition to their occurrence as extrusive

584 flows, nakhlites and chassignites share many features as regards their sulfide assemblages, i.e.  
585 metal-deficient pyrrhotite predominating over pentlandite and Cu-sulfides. Our pyrrhotite  
586 compositions overlap the pyrrhotite compositions so far published for nakhlites (Table 4). Chevrier  
587 et al. (2011) suggested that nakhlite pyrrhotites experienced deuteric oxidation resulting from water  
588 dissociation and devolatilization of intercumulus melts. Deuteric oxidation results from  
589 accumulation of Fe<sup>3+</sup>-rich minerals raising oxygen fugacity in the latest magmatic differentiates  
590 after massive precipitation of Fe<sup>2+</sup>-rich minerals such as olivine (e.g. Czamanske and Wones 1973).  
591 McCubbin and Nekvasil (2008), McCubbin et al. (2013) and Giesting et al. (2015) suggested that  
592 degassing changed significantly the H<sub>2</sub>O content of the interstitial magma in the Chassigny  
593 cumulate during uplift and eruption or near-surface emplacement. According to these authors,  
594 retrograde boiling and degassing may increase oxygen fugacity through the loss of hydrogen while  
595 H<sub>2</sub>O losses may account for the lack of biotite and amphibole in the intergranular mesostasis of the  
596 Chassigny meteorite. McCubbin and Nekvasil (2008) and McCubbin et al. (2013) interpreted the  
597 Cl-enrichment of intercumulus apatites (compared to the olivine-hosted F-rich apatite  
598 compositions) as resulting from addition of an exogenous Cl-rich fluid to the intercumulus regions  
599 of the Chassigny meteorite above 700 °C. This late-percolating fluid may also have disturbed  
600 pyrrhotite compositions if it was introduced into the cumulate horizon sampled by Chassigny  
601 immediately after formation and accumulation of the cumulus olivine.

602 Another potential source of alteration of igneous pyrrhotite composition is assimilation of  
603 crustal sulfur coeval driven by magmatic crystallization (Assimilation-Fractional Crystallization  
604 process), as suggested by Franz et al (2014) for nakhlites. These authors found Mass Independent  
605 Fractionation (MIF) in the S isotopic composition of sulfides chemically extracted from Nakhla  
606 ( $\Delta^{33}\text{S} = -0.08 \text{ ‰}$ ), and Miller Range (MIL) 03346 ( $\Delta^{33}\text{S} = 0.434 \pm 0.008 \text{ ‰}$  to  $-0.5386 \pm 0.008$   
607  $\text{‰}$ ). SIMS in-situ analyses confirmed these bulk-rock analyses of MIF, within the error of the  
608 chemical extraction analysis for Nakhla, and more variable values for individual pyrrhotite of MIL  
609 03346 ( $-0.306 \pm 0.13 \text{ ‰} < \Delta^{33}\text{S} < -1.116 \pm 0.13 \text{ ‰}$ ). Franz et al (2014) concluded that sulphur salts

610 (Ca sulfates) or sulphur-bearing fluids were assimilated by parental melts at the time the nakhlite  
611 flows were extruded. If valid for nakhlites, this model of exogeneous sulfur assimilation at the  
612 magmatic stage is plausible for Chassigny that was part of a subaerial flow erupted on the S-rich  
613 Martian surface. However, the very small size of igneous pyrrhotite grains made in-situ SIMS  
614 analyses of S isotope compositions impossible (J. Farquhar, personal communication to J.-P.  
615 Lorand). Only a bulk analysis of the Chrome Reducible Sulfide fraction is available ( $\Delta^{33}\text{S} = 0.004$   
616  $\pm 0.008$  ‰; Frantz et al, 2014), which, however is a mixture of both igneous metal-deficient  
617 pyrrhotite and hydrothermal pyrite. Fig. 10 clearly shows that the assemblage Ca sulfates + a  
618 metal-deficient pyrrhotite ( $\text{Fe}_{0.88}\text{S}$ ) produce the same oxidizing conditions (FMQ + 1.5 log unit) as  
619 those defined by the sulfidation reaction of olivine. One may speculate that, because of its  
620 exceedingly low modal volume, Chassigny pyrrhotite reequilibrated under the redox conditions  
621 imposed by assimilation of sulfates, without reequilibrating for S isotopic compositions. Of course,  
622 such a reequilibration is assumed to have started before isolation of olivine-hosted melt inclusions  
623 inside olivine.

## 624 625 **CONCLUSION** 626

627 Like other Martian basalts so far studied for sulfur and strongly chalcophile elements (i.e.  
628 PGEs), the parental melt of the Chassigny dunitic cumulate achieved sulfide-saturation at a late  
629 stage of its crystallization, after olivine and chromite precipitation. Igneous sulfides precipitated in-  
630 situ as magmatic sulfide melt of low-Ni pyrrhotite bulk composition, either inside porphyritic  
631 silicate melt inclusions in olivine or as polyhedral or near-spherical blebs in intergranular spaces  
632 between cumulus olivine. The igneous pyrrhotite displays Ni/Fe ratios within the range expected  
633 for equilibration with the coexisting olivine at igneous temperatures.

634 Chassigny sulfides bear imprints of each petrogenetic process experienced by the Chassigny  
635 meteorite. Once segregated, the pyrrhotite experienced a late-magmatic reequilibration of its metal-

636 to-sulfur ratios toward a general formula  $M_{0.88\pm 0.01}S$  ( $M = Fe+Ni+Co+Cu+Mn$ ). This reequilibration  
637 may result from retrograde boiling, volatile loss, or contamination by crustal sulfates, perhaps  
638 driven by post-cumulus circulation of late-magmatic differentiated melts.

639 Hydrothermal fluids operated pervasively over different temperatures well after complete  
640 cooling of the Chassigny dunite. Magmatic pyrrhotite was converted to pyrite along with other  
641 accessory sulfides (e.g. millerite), in line with low-temperature precipitation of Ca sulfate + Ca  
642 carbonate deposition. The shock that ejected the Chassigny meteorite from Mars generated post-  
643 shock temperatures high enough (300°C) to anneal and rehomogenize Ni inside pyrrhotite while  
644 pyrite blebs were fractured and disrupted into subgrains by shock metamorphism. Owing to its high  
645 density of fractures, pyrite was preferentially oxidized on Earth compared to pyrrhotite.

646 Hydrothermal alteration and shock metamorphism generated strong heterogeneity inside the  
647 Chassigny meteorite. This is demonstrated by the distribution of pyrite, marcasite, and an FeS  
648 phase (troilite) between each piece of the meteorite investigated so far for Fe-Ni sulfides.

649

650 **Acknowledgement** Financial funding was provided by a INSU 2014-PNP grant (JPL). The authors  
651 thank Michel Fialin (Camparis) for his help with electron microprobe analyses.

652

## 653 REFERENCES CITED

654

655 Barton, P.B. (1970) Sulfide petrology. Mineral Society of America Special Paper, 3, 187-198.

656

657 Baumgartner, R., Fiorentini, M.L., Lorand, J.-P., Baratoux, D., Zaccarini, F., Ferrière, L., Prasek,  
658 M., and Sener, K. (2017a) The role of sulfides in the fractionation of highly siderophile and  
659 chalcophile elements during the formation of Martian shergottite meteorites. *Geochimica*  
660 *Cosmochimica Acta*, 210, 1-24.

661

662 Baumgartner, R.J., Fiorentini, M.L., Baratoux, D., Ferrière, L., Locmelis, M., Tomkins, A. and

663 Sener, A. K. (2017b) The variability of ruthenium in chromite from Chassignite and olivine-  
664 phytic shergottite meteorites: new insights into the behavior of PGE and sulfur in Martian  
665 magmatic systems. *Meteoritics and Planetary Science*, 52, 333–350  
666

667 Belzile, N., Chen, Y. W., Cai, C. F. and Li, Y. (2004) A review on pyrrhotite oxidation. *Journal of*  
668 *Geochemical Exploration*, 84, 65–76.  
669

670 Beck, P., Gillet, P., Barrat, J.-A., Wadhwa, M., Greenwood, R. C., Franchi, I. A., Bohn, M.,  
671 Cotten, J., Van de Moortele, B. and Reynard, B. (2006) Petrography and geochemistry of the  
672 Chassignite Northwest Africa 2737 (NWA 2737). *Geochimica Cosmochimica Acta*, 70,  
673 2127–2139.  
674

675 Bogard, D. D., and Garrison, D. H. (2008)  $^{39}\text{Ar}$ – $^{40}\text{Ar}$  age and thermal history of Martian dunite  
676 NWA 2737. *Earth and Planetary Science Letters*, 273, 386–392.  
677

678 Boctor, N.Z., Wang, J., Alexander, C.M.O., Hauri, E. (2006) Volatile abundances and hydrogen  
679 isotope signatures of melt inclusions and nominally anhydrous minerals in the Chassignites  
680 and ALH84001 (abs#1412). *Lunar Planet. Sci. XXXVII Lunar Planetary Institute, Houston*  
681

682 Brandon, A.D., Walker, R.J., Morgan, J., and Goles, G.G. (2000) Re–Os isotopic evidence for  
683 early differentiation of the Martian mantle. *Geochimica Cosmochimica Acta*, 64, 4083–4095.  
684

685 Brandon, A.D., Puchtel I. S., Walker, R. J., Day, J.M.D., Irving, A.J. and Taylor L.A. (2012)  
686 Evolution of the Martian mantle inferred from the  $^{187}\text{Re}$ – $^{187}\text{Os}$  isotope and highly  
687 siderophile element abundance systematics of shergottite meteorites. *Geochimica*  
688 *Cosmochimica Acta*, 76, 206–235.

689

690 Brenan, J.M. (2003) Effects of  $f_{O_2}$ ,  $f_{S_2}$ , temperature, and melt composition on Fe-Ni exchange  
691 between olivine and sulfide liquid: Implications for natural olivine–sulfide assemblages.  
692 *Geochimica Cosmochimica Acta*, 67, 2663-2681.

693

694 Brenan, J.M., Bennett, N.R. and Zajacz, Z. (2016) Experimental results on fractionation of the  
695 highly siderophile elements (HSE) at variable pressures and temperatures during planetary  
696 and magmatic differentiation. *Review in Mineralogy and Geochemistry*, 81, 1–88.

697

698 Bridges, J.C., Catling, D.C., Saxton, J.M., Swindle, T.D., Lyon, I., and Grady, M.M. (2001)  
699 Alteration assemblages in Martian meteorites: Implications for near-surface processes. *Space  
700 Science Review*, 96, 365-392.

701

702 Chandra, A.P. and Gerson, A.R. (2011) Pyrite (FeS<sub>2</sub>) oxidation: A sub-micron synchrotron  
703 investigation of the initial steps. *Geochimica Cosmochimica Acta*, 75, 6239–6254.

704

705 Chevrier, V., Lorand, J.-P. and Sautter, V. (2011) Sulfide petrology of four Nakhrites (NWA817,  
706 NWA998, Nakhla, Governador Valadares). *Meteoritics and Planetary Science*, 46, 769-784.

707

708 Cox, S.F. (1987) Flow mechanisms in sulphide minerals. *Ore Geology Review*, 2, 133-7.

709

710 Craig, J.R. (1973) Pentlandite-pyrrhotite and other low-temperature relations in the Fe-Ni-S  
711 system. *American Journal of Science*, 273, 496-510.

712

713 Craig, J. R. and Kullerud, G. (1969) Phase relations in the Cu-Fe-Ni-S system and their  
714 applications to magmatic ore deposits. *Economic Geology Monography* 4, 344-358.

715

716 Craig, J. R. and Vokes, F. M. (1993) The metamorphism of pyrite and pyritic ores: an overview.  
717 Mineralogical Magazine, 57, 3–18.

718

719 Czamanske, G.K. and Wones, D.R. (1973) Oxidation during magmatic differentiation, Finnmarka  
720 complex, Oslo area, Norway: Part 2. The mafic silicates. Journal of Petrology, 14, 349-380.

721

722 Day, J.M.D., Taylor, L. A., Floss, C. and McSween, H. Y. Jr. (2006) Petrology and chemistry of  
723 MIL 03346 and its significance in understanding the petrogenesis of Nakhilites on Mars.  
724 Meteoritics and Planetary Science, 41, 581-606.

725

726 Dehouck, E., Chevrier, V., Gaudin, A., Mangold, N., Mathé, P.E. and Rochette, P. (2012)  
727 Evaluating the role of sulfide-weathering in the formation of sulfates or carbonates on Mars.  
728 Geochimica et Cosmochimica Acta, 90, 47–63.

729

730 Delaney, J.S. and Dyar, M.D. (2001) Magmatic magnetite in Martian meteorite melt inclusions  
731 from Chassigny (abs). Meteoritics and Planetary Science, 36, A48.

732

733 Ding, S., Dasgupta, R., Lee, C. T. A and Wadhwa, M. (2015) New bulk sulfur measurements of  
734 Martian meteorites and modeling the fate of sulfur during melting and crystallization—  
735 Implications for sulfur transfer from Martian mantle to crust–atmosphere system. Earth and  
736 Planetary Science Letters, 409, 157–167.

737

738 Eggler, D.H. and Lorand, J.-P. (1993) Mantle sulfide oxybarometry. Geochimica et  
739 Cosmochimica Acta, 57, 2213-2222.

740

741 Etschmann, B., Pring, A., Putnis, A., Grguric, B. A. and Studer, A. (2004) A kinetic study of the  
742 exsolution of pentlandite (Ni,Fe)<sub>9</sub>S<sub>8</sub> from the monosulfide solid solution (Fe,Ni)S. *American*  
743 *Mineralogist*, 89, 39-50.

744

745 Foley, C.N., Economou, T. and Clayton, R. N. (2003) Final chemical results from the Mars  
746 Pathfinder Alpha Proton X-ray Spectrometer. *Journal of Geophysical Research* 108, 8096,  
747 doi:10.1029/2002JE002019.

748

749 Farquhar, J., Savarino, J., Jackson, T.L., Thiemens, M.H. (2000) Evidence of atmospheric sulphur  
750 in the Martian regolith from sulphur isotopes in meteorites. *Nature*, 404, 50-52.

751

752 Farquhar, J., Kim, S.-T. and Masterson, A. (2007) Implications from sulphur isotopes of the  
753 Nakhla meteorite origin of sulfate on Mars. *Earth and Planetary Science Letters*, 264, 1–8.

754

755 Filiberto, J. (2008) Experimental constraints on the parental liquid of the Chassigny meteorite: A  
756 possible link between the Chassigny meteorite and a Martian Gusev basalt. *Geochimica et*  
757 *Cosmochimica Acta*, 72, 690-701.

758

759 Fleet, M.E. (1978) The pyrrhotite–marcasite transformation. *Canadian Mineralogist*, 16, 31–35.

760

761 Floran, R.J., Prinz, M., Hlava, P.F., Keil, K., Nehru, C.E. and Hinthorne, J.R. (1978) The  
762 Chassigny meteorite. *Geochimica et Cosmochimica Acta*, 42, 1213-1229.

763

764 Franz, H.B., Kim, S.T., Farquhar, J., Day, J.M.D., Economos, R., McKeegan K.D., Schmitt, A.K.,  
765 Irving, A.J., Hoek, J. and Dottin, J. (2014) Isotopic links between atmospheric chemistry and  
766 the deep sulphur cycle on Mars. *Nature*, 508, 364–368.

767

768 Gattacceca, J., Hewins, R.J., Lorand, J.-P., Rochette, P., Lagroix, F., Cournède, C., Uehara, M.,  
769 Pont, S., Sautter, V., Scorzelli, R.B., Hombourger, C., Munayco, P., Zanda, B. and Chennaoui,  
770 H. (2013) Opaque minerals, magnetic properties and paleomagnetism of the Tissint Martian  
771 meteorite. *Meteoritics and Planetary Science*, 48, 1919-1936.

772

773 Giesting, P.A., Schwenzer, S.P., Filiberto, J., Starkey, N.A., Franchi, I.A., Treiman, A.H., Tindle,  
774 A. and Grady, M.M. (2015) Igneous and shock processes affecting chassignite amphibole  
775 evaluated using chlorine/water partitioning and hydrogen isotopes. *Meteoritics and Planetary  
776 Science*, 50, 433–460.

777

778 Gibson, E.K., Moore, C.B., Primus, T.M. and Lewis, C.F. (1985) Sulfur in achondritic meteorites.  
779 *Meteoritics and Planetary Science*, 20, 503-511.

780

781 Greenwood, J.P., Mojzsis, S.J. and Coath, C.D. (2000a) Sulfur isotopic compositions of individual  
782 sulfides in Martian meteorites ALH84001 and Nakhla: implications for crust-regolith exchange  
783 on Mars. *Earth and Planetary Science Letters*, 184, 23-30.

784

785 Greenwood, J.P., Riciputi, L.R., McSween, H.Y. and Taylor, L.A. (2000b) Modified sulfur  
786 isotopic compositions of sulfides in the Nakhrites and Chassigny. *Geochimica et Cosmochimica  
787 Acta*, 64, 1121-1131.

788

789 Hall, A.J. (1986) Pyrite-pyrrhotine redox reactions in nature. *Mineralogical Magazine*, 50, 223-

790

791 Harries, D., Pollok, K. and Langenhorst, F. (2013) Oxidative dissolution of 4C- and Nc pyrrhotite:  
792 intrinsic reactivity differences, pH dependence, and the effect of anisotropy. *Geochimica et  
793 Cosmochimica Acta*, 102, 23–44.

794

795 Harvey, R.P., McSween HYJr (1992) Petrogenesis of the nakhlite meteorites: Evidence from  
796 cumulate mineral zoning. *Geochimica et Cosmochimica Acta* 56, 1655–1663.

797 Hayes, S.M., Root R.A., Perdrial, N., Maier, R.M. and Chorover, J. (2014) Surficial weathering of  
798 iron sulfide mine tailings under semi-arid climate. *Geochimica et Cosmochimica Acta*, 141,  
799 240–257.

800 He, Q., Xiao, L., Hsu, W., Balta, J.B., McSween, H.Y. and Liu, Y. ( 2013) The water content and  
801 parental magma of the second Chassignite NWA 2737: Clues from trapped melt inclusions in  
802 olivine. *Meteoritics and Planetary Science*, 48, 474–492.

803 Herd, C.D.K., Borg, L., Jones, J.H. and Papike, J. J. (2002) Oxygen fugacity and geochemical  
804 variations in the Martian basalts: Implications for Martian basalt petrogenesis and the oxidation  
805 state of the upper mantle of Mars. *Geochimica et Cosmochimica Acta*, 66, 2025–2036.

806

807 Hewins, R.H., Zanda, B., Pont, S., Humayun, M., Assayag, N. and Cartigny, P. ( 2015) Northwest  
808 Africa 8694, a ferroan Chassignite (abstract # 2249). 46th Lunar and Planetary Science  
809 Conference. CD-ROM.

810

811 Holwell, D.A., Adeyemia, Z., Warda, L.A., Smith, D.J., Graham, S.D., McDonald, I. and Smith,  
812 J.W. (2017) Low temperature alteration of magmatic Ni-Cu-PGE sulfides as a source for  
813 hydrothermal Ni and PGE ores: A quantitative approach using automated mineralogy. *Ore  
814 Geology Review*, 91, 718-740.

815

816 Huminicki, D.M.C. and Rimstidt, J.D. (2009) Iron oxyhydroxide coating of pyrite for acid mine  
817 drainage control. *Applied Geochemistry*, 24, 1626-1634.

818

819 Imae, N. and Ikeda, Y. (2007) Petrology of the Miller Range 03346 nakhlite in comparison with  
820 the Yamato-000593 nakhlite. *Meteoritics and Planetary Science*, 42,171-184.  
821

822 Janzen, M.P., Nicholson, R.V. and Scharer, J.M. (2000) Pyrrhotite reaction kinetics: reaction rates  
823 for oxidation by oxygen, ferric iron, and for nonoxidative dissolution. *Geochimica et*  
824 *Cosmochimica Acta*, 64, 1511–1522.

825 Jerz, J.K. and Rimstidt, J.D. (2004) Pyrite oxidation in moist air. *Geochimica et Cosmochimica*  
826 *Acta*, 68, 701–714.  
827

828 Johnson, M.C., Rutherford, M.J. and Hess, P.C. (1991) Chassigny petrogenesis: Melt  
829 compositions, intensive parameters, and water contents of Martian magmas. *Geochimica et*  
830 *Cosmochimica Acta*, 55, 349-366.  
831

832 Kanipayacharoen, W. and Boudreau, A.E. (2013) Sulfide-associated mineral assemblages in the  
833 Bushveld complex, South Africa: platinum-group element enrichment by vapor refining by  
834 chloride-carbonate fluids. *Mineralogical Deposita*, 48, 193-210.  
835

836 Kerber, L., Forget, F. and Wordsworth, R. (2015) Sulfur in the early Martian atmosphere  
837 revisited: Experiments with a 3-D Global Climate Model. *Icarus*, 261, 133–148.  
838

839 King, P.L. and McLennan, S.M. (2010) Sulfur on Mars. *Elements*, 6,107-112.  
840

841 Kissin, S.A. and Scott, S.D. (1982). Phase relations involving pyrrhotite below 350°C. *Economic*  
842 *Geology*, 77, 1739-1755.  
843

844 Langenhorst, F. and Greshake, A. (1999) A transmission electron microscope study of Chassigny:

845 Evidence for strong shock metamorphism. *Meteoritics and Planetary Science*, 34, 43-48.

846

847 Leshin, L.A., Epstein, S. and Stolper, E. M. (1996) Hydrogen isotope geochemistry of SNC  
848 meteorites. *Geochimica Cosmochimica Acta*, 60, 2635–2650.

849

850 Liu, R., Wolfe, A.L., Dzombak, D.A., Horwitz, C.P., Stewart, B.W. and Capo, R.C. (2009)  
851 Controlled electrochemical dissolution of hydrothermal and sedimentary pyrite. *Applied*  
852 *Geochemistry*, 24, 836–842.

853

854 Lorand, J.-P., Alard, O. (2011) Pyrite tracks assimilation of crustal sulfur in some Pyrenean  
855 Iherzolites. *Mineralogy Petrology*, 101, 115-128.

856

857 Lorand, J.-P., Barat, J.-A., Chevrier, V., Sautter, V. and Pont, S. (2012) Metal-saturated sulfide  
858 assemblages in Chassignite NWA 2737; evidence for impact-related sulfur devolatilisation.  
859 *Meteoritics and Planetary Science*, 47, 1830-1841.

860

861 Lorand, J.-P., Chevrier, V. and Sautter, V. (2005) Sulfide mineralogy and redox conditions in  
862 some Shergottites. *Meteoritics and Planetary Science* , 40, 1257-1272.

863

864 Lorand, J.-P., Hewins, R. H., Pont, S., Zanda, B., Humayun, M., Nemchin, A . and others (2015)  
865 Nickeliferous pyrite tracks late hydrothermalism in Martian regolith breccia NWA 7533.  
866 *Meteoritics and Planetary Science*, 50, 2099-2120.

867

868 Malavergne, V., Guyot, F., Benzerara, K. and Martinez, I. (2002) Descriptions of new shock-  
869 induced phases in the Shergotty, Zagami, Nakhla and Chassigny meteorites. *Meteoritics and*  
870 *Planetary Science*, 36, 1297-1305.

871

872 Mavrogènes, J.A., O'Neill, H.S.C. (1999) The relative effects of pressure, temperature and  
873 oxygen fugacity on the solubility of sulfide in mafic magmas. *Geochimica et Cosmochimica*  
874 *Acta*, 63, 1173–1180.

875

876 McClay, K.R. and Ellis, P.G. (1983) Deformation and recrystallization of pyrite. *Mineralogical*  
877 *Magazine* 47, 527-538.

878

879 McCubbin, F. M. and Nekvasil, H. (2008) Maskelynite-hosted apatite in the Chassigny meteorite:  
880 Insights into late-stage magmatic volatile evolution in Martian magmas. *American*  
881 *Mineralogist*, 93, 676–684.

882 McCubbin, F.M., Nekvasil, H., Harrington, A.D., Elardo, S.M. and Lindsley, D. H. (2008)  
883 Compositional diversity and stratification of the Martian crust: Inferences from crystallization  
884 experiments on the microbasalt Humphrey from Gusev crater, Mars. *Journal of Geophysical*  
885 *Research-Planets* 113:E11013. doi:10.1029/2008JE003165

886 McCubbin, F.M., Elardo, S.M. and Shearer, C.K. Jr (2013) A petrogenetic model for the  
887 comagmatic origin of Chassignites and Nakhrites: Inferences from chlorine-rich minerals,  
888 petrology and geochemistry. *Meteoritics and Planetary Science*, 48, 819-853.

889

890 McSween, H.Y. Jr (2001) The rocks of Mars, from far and near. *Meteoritics and Planetary*  
891 *Science*, 37,7-25.

892

893 McSween, H.Y. Jr and McLennan, S.M. (2014). *Mars. Treatise on Geochemistry*, 2nd edition,  
894 Chapter 2.10, . Editor: Executive Editors: Heinrich D. Holland and Karl K. Turekian, pp 251-  
895 282.

896

897 McSween, H.Y. Jr and Treiman A.H. (1998) *Planetary Materials. Martian Meteorites. Reviews in*

898 Mineralogy (Papike J. J. ed.). Chapter 36, 6-1.

899

900 Meyer, C. (2012) The Martian Meteorite Compendium. *Astromaterials Research & Exploration*  
901 *Science (ARES)*. <http://curator.jsc.nasa.gov/antmet/mmc/>.

902

903 Mikhlin, Y.L. and Tomashevich, Y. (2005) Pristine and reacted surfaces of pyrrhotite and  
904 arsenopyrite as studied by X-ray absorption near-edge structure spectroscopy. *Physics*  
905 *Chemistry of Minerals*, 32,19–27.

906

907 Morikawa, N., Mikouchi, T., Koizumi, E., Sukiya, K., Miyamoto, M. (2006) Determination of  
908 the Fe oxidation state of Chassigny keasurtite: A microXANES spectroscopic study.  
909 *Meteoritics and Planetary Science*, 41, 1321-1329.

910

911 Misra, K. and Fleet, M.E. (1973). The chemical composition of synthetic and natural pentlandite  
912 assemblages. *Economic Geology*, 68, 518-539.

913

914 Naldrett, A.J. (2005). History of our understanding of magmatic Ni–Cu sulfide deposits. *Canadian*  
915 *Mineralogist*, 43, 2069–2098.

916

917 Murowchick, J.B. (1992) Marcasite inversion and the petrographic determination of pyrite  
918 ancestry. *Economic Geology*, 87,1141–1152.

919

920 Mycroft J. R., Nesbitt H. W. and Pratt A. R. (1995) X-ray photoelectron and Auger electron  
921 spectroscopy of air-oxidized pyrrhotite: Distribution of oxidized species with depth.  
922 *Geochimica et Cosmochimica Acta*, 59, 721–733.

923

924 Naldrett, A.J., Craig, J.R. and Kullerud, G. (1967) The central portion of the Fe-Ni-S system and

925 its bearing on pentlandite exsolution in iron-nickel sulfide ores. *Economic Geology*, 62, 826-  
926 847.

927

928 Nekvasil, H., Filiberto, J., McCubbin, F. and Lindsley D.H. (2007) Alkalic parental magmas for  
929 Chassignites? *Meteoritics and Planetary Science*, 42, 979-992.

930

931 Nekvasil, H., McCubbin, F.M., Harrington, A., Elardo, S. and Lindsley D.H. (2009) Linking the  
932 Chassigny meteorite and the Martian surface rock Backstay: Insights into igneous crustal  
933 differentiation processes on Mars. *Meteoritics and Planetary Science*, 44, 853–869.

934 Nesbitt, H.W., Bancroft, G.M., Pratt, A.R. and Scaini, M.J. (1998) Sulfur and iron surface states  
935 on fractured pyrite surfaces. *American Mineralogist*, 83, 1067–1076.

936

937 Nyquist, L.E, Bogard, D. D., Shih, C.Y., Greshake, A., Stöffler, D. and Eugster, O. (2001) Ages  
938 and geological histories of Martian meteorites. *Space Science Reviews*, 96,105–164.

939

940 Papike, J.J., Karner, J.M., Shearer, C.M. and Burger, P.V. (2009) Silicate mineralogy of Martian  
941 meteorites. *Geochimica Cosmochimica Acta*, 73,7443-7485.

942

943 Parat, F, Holz, F. and Streck, M.J. (2011) Sulfur-bearing Magmatic Accessory Minerals. Review  
944 in *Mineralogy and Geochemistry*, 73, pp. 285-333.

945

946 Pistorlet (1816) The circumstances of the Chassigny meteorite shower. *Annales Chimie et*  
947 *Physique (Paris)* v. 1, pp 45-48.

948

949 Pratt, A.R., Muir, I.J. and Nesbitt, H.W. (1994) X-ray photoelectron and Auger electron  
950 spectroscopic studies of pyrrhotite and mechanism of air oxidation. *Geochimica et*

951 Cosmochimica Acta, 58, 827–841.

952

953 Raghavan, V. (2004). Fe-Ni-S (Iron-Nickel-Sulfur) system. Journal of Phase Equilibrium  
954 Diffraction, 25, 373–381.

955

956 Reid, A.M. and Bunch, T. E. (1975) The Nakhilites part II: Where, when and how. Meteoritics, 10,  
957 317.

958

959 Rickard, D. and Luther, G.W. (2007) Chemistry of Iron Sulfides, 107, 514-562.

960

961 Rimstidt, J.D. and Vaughan, D.J. (2003) Pyrite oxidation: a state-of-the-art assessment of the  
962 reaction mechanism. Geochimica et Cosmochimica Acta, 67, 873–880.

963

964 Shearer, C.K., Layne, G.D., Papike, J.J. and Spilde, M.N. (1996) Sulfur isotopic systematics in  
965 alteration assemblages in Martian meteorite Allan Hills 84001. Geochimica et Cosmochimica  
966 Acta, 60, 2921–2926.

967

968 Skinner, W.M., Nesbitt, H.W. and Pratt, A.R. (2004) XPS identification of bulk hole defects and  
969 iterant Fe 3d electrons in natural trolite (FeS). Geochimica et Cosmochimica Acta, 68, 2259–  
970 2263.

971

972 Tian, F., Mark, W., Claire, B., Jacob, D., Haqq, M., Megan Smith, Crisp, D.C., Catling, D.,  
973 Zahnle, K. and Kasting, J.F. (2010) Photochemical and climate consequences of sulfur  
974 outgassing on early Mars. Earth and Planetary Science Letters, 295, 412–418.

975

976 Thornber, M.R. (1975) Supergene alteration of sulphides. I. Chemical model based on massive  
977 nickel sulphide deposits at Kambalda, Western Australia. Chemical Geology, 15, 1–14.

- 978 Thomas, J.E., Jones, C.F., Skinner, W.M. and Smart, R.St. C. (1998) The role of surface sulfur  
979 species in the inhibition of pyrrhotite dissolution in acid conditions. *Geochimica et*  
980 *Cosmochimica Acta*, 62, 1555– 1565.
- 981
- 982 Thomas, J.E., Skinner, W.M., Smart, R.St. C. (2001) A mechanism to explain sudden changes in  
983 rates and products for pyrrhotite dissolution in acid solution. *Geochimica et Cosmochimica*  
984 *Acta*, 65, 1–12.
- 985
- 986 Todd, E.C., Sherman, D.M. and Purton, J.A. (2003) Surface oxidation of pyrite under ambient  
987 atmospheric and aqueous (pH = 2 to 10) conditions: electronic structure and mineralogy from  
988 X-ray absorption spectroscopy. *Geochimica et Cosmochimica Acta*, 67, 881–893.
- 989
- 990 Toulmin, P. and Barton, P.B. (1964) A thermodynamic study of pyrite and pyrrhotite. *Geochimica*  
991 *et Cosmochimica Acta*, 68, 641-671.
- 992
- 993 Treiman, A.H., Gleason, J.D., and Bogard, D.D. (2000) The SNC meteorites are from Mars.  
994 *Planetary Space Sciences*, 48, 1213–1230.
- 995 Treiman, A.H., Dyar, M. D., McCanta, M., Noble, S.K. and Pieters, C.M. (2007) Martian dunite  
996 NWA 2737: Petrographic constraints on geological history, shock events, and olivine color.  
997 *Journal of Geophysical Research- Planets* 112:E04002. doi:10.1029/2006JE002777.
- 998
- 999 Treiman, A.H. and Irving, A.J. (2008) Petrology of Martian meteorite Northwest Africa 998.  
1000 *Meteoritics and Planetary Science*, 43, 829–854.
- 1001
- 1002 Varela, M.E., Kurat, G., Bonnín-Mosbah, M., Clocchiatti, R. and Massare, D. (2000) Glass-  
1003 bearing inclusions in olivine of the Chassigny achondrite: Heterogeneous trapping at sub-

- 1004 igneous temperatures. *Meteoritics and Planetary Science*, 35, 39-52.
- 1005
- 1006 Wadhwa, M. and Crozaz, G. (1995a) Trace and minor elements in minerals of Nakhilites and  
1007 Chassigny: Clues to their petrogenesis. *Geochimica et Cosmochimica Acta*, 59, 3629-3647.
- 1008
- 1009 Watmuff, I.G. (1974) Supergene alteration of the Mt Windara nickel sulfides ores deposits,  
1010 Western Australia. *Mineralium Deposita*, 9, 199-211.
- 1011 Wentworth, S.J. and Gooding, J.L. (1994) Carbonates and sulfates in the Chassigny meteorite:  
1012 Further evidence for aqueous chemistry on the SNC parent planet. *Meteoritics and Planetary  
1013 Science*, 29, 860-863.
- 1014
- 1015 Wang, Z. and Becker, H. (2017) Chalcophile elements in Martian meteorites indicate low sulfur  
1016 content in the Martian interior and a volatile element-depleted late veneer. *Earth Planetary  
1017 Science Letters*, 463, 56–68.
- 1018
- 1019 Williamson, M.A. and Rimstidt, J.D. (1994) The kinetics and electrochemical rate determining  
1020 step of aqueous pyrite oxidation. *Geochimica Cosmochimica Acta* 58, 5443–5454.
- 1021
- 1022 Zurfluh, F.L., Beda, A., Hofmann, Gnos, E. and Eggenberger, U. (2013) “Sweating meteorites”—  
1023 Water-soluble salts and temperature variation in ordinary chondrites and soil from the hot  
1024 desert of Oman. *Meteoritics and Planetary Science*, 48, 1958–1980.

1025

1026 **Figure captions**

1027

1028 FIGURE 1: Low-magnification backscattered electron (BSE) image of the Chassigny meteorite  
1029 showing the distribution of Fe-Ni sulfides (white star) in one of the two polished mounts

1030 investigated in this study.

1031

1032 FIGURE 2: Microphotographs of Chassigny sulfides. 2a: pyrrhotite included in an olivine-hosted  
1033 melt inclusion (reflected light optical microscope). 2b: intergranular pyrrhotite hosted in a feldspar  
1034 pocket enclosing euhedral chromite (reflected light optical microscope); 2c: detail of Fig. 2b  
1035 showing a two-phase (pyrrhotite + pentlandite) ellipsoidal magmatic sulfide grain associated with  
1036 a euhedral apatite inclusion inside the feldspar glass (BSE image). 2d: intergranular pyrrhotite (+  
1037 pentlandite) at triple junction of olivine crystals (reflected light optical microscope). 2e:  
1038 polyhedral intergranular pyrrhotite (+ pentlandite) showing convex-inward grain boundaries (BSE  
1039 image). 2f: highly fractured, rounded pyrite grain showing incipient replacement by an NiS phase  
1040 (BSE image). 2g: intergranular pyrite showing formation of subgrains (BSE image). 2h: rounded  
1041 and highly granulated pyrite (white) showing incipient alteration in Fe oxyhydroxides (reflected  
1042 light optical microscope; oil immersion objective). Ol: olivine; Opx: orthopyroxene; Chr:  
1043 chromite; Ap: apatite; Amph: amphibole; Fs: feldspar; Po: pyrrhotite; Py: pyrite; Pn: pentlandite;  
1044 Fe oxhyd: Fe oxyhydroxide.

1045

1046 FIGURE 3: Distribution of sulfide grain sizes in the Chassigny meteorite.

1047

1048 FIGURE 4: Metal-to-sulfur atomic ratios (M/S;  $M = \text{Fe} + \text{Ni} + \text{Co} + \text{Cu} + \text{Mn}$ ) of Chassigny  
1049 pyrrhotite (WDS analyses only).  $\text{Fe}_7\text{S}_8$  : monoclinic pyrrhotite;  $\text{Fe}_9\text{S}_{10}$  : hexagonal pyrrhotite  
1050 (Kissin and Scott, 1982)

1051

1052 FIGURE 5: Ni concentrations (wt%) in pyrrhotite and pyrite (WDS analyses only). N = number of  
1053 analyses.

1054

1055 FIGURE 6: Metal-to-sulfur atomic ratio vs. oxygen contents for pyrrhotite and pyrite (WDS

1056 analyses only).

1057

1058 FIGURE 7: Plot of Chassigny pyrrhotite compositions (squares) in the Fe-Ni-S system at 300°C.  
1059 Compositional range and phase relationships of Mss (monosulfide solid solution) from Naldrett et  
1060 al (1967), Craig (1973) and Rhagavan, (2004). Fe<sub>7</sub>S<sub>8</sub>: monoclinic pyrrhotite; Fe<sub>9</sub>S<sub>10</sub>: hexagonal  
1061 pyrrhotite; FeS: troilite (Kissin and Scott, 1982).

1062

1063 FIGURE 8: Plot of the mean composition of Chassigny pyrrhotite (M<sub>0.88</sub>S; white star) in the log  
1064 fS<sub>2</sub>-T diagram for the Fe-S-O system (after Lorand et al., 2005 and Chevrier et al., 2011).  
1065 Pyrrhotite isopleths of metal-to-sulfur atomic ratios, pyrrhotite iron (Fe-Po) and sulfur vapor-sulfur  
1066 liquid (Svap-Sliq) reaction curves from Toulmin and Barton (1964). The curves labeled with  
1067 oxygen fugacity are for the reaction: 3FeS + 2O<sub>2</sub> = Fe<sub>3</sub>O<sub>4</sub> + S<sub>2</sub> (pyrrhotite-magnetite equilibrium);  
1068 FMQ-Po buffer from Eggler and Lorand (1993). We present two possible subsolidus evolutions for  
1069 the Chassigny igneous pyrrhotite. Path A assumes subsolidus re-equilibration controlled by the  
1070 FMQ-Po buffer curve (see text for description of the buffer). Note that path A precludes pyrrhotite  
1071 M/S ratios < 0.91. Path B assumes cooling of the Chassigny pyrrhotite at constant M/S ratio. Path  
1072 A should trigger pyrite exsolution at high temperature, and then increasing M/S ratios in the co-  
1073 existing pyrrhotite down to 0.91.

1074

1075 FIGURE 9: Low-temperature (135°C) phase relationships in the Fe-Ni-S system (wt %) after Craig  
1076 (1973) and Rhagavan (2004)(wt%). This diagram illustrates a putative reaction path (arrow) at  
1077 decreasing Fe/Ni ratio producing pyrite + NiS from the igneous sulfide assemblage of Chassigny  
1078 (pyrrhotite + pentlandite). Mss1 and Mss 2: compositional field of monosulfide solid solutions 1  
1079 and 2 from Craig (1973). Py: pyrite; Mpo: monoclinic pyrrhotite (Fe<sub>7</sub>S<sub>8</sub>); Hpo: hexagonal  
1080 pyrrhotite (Fe<sub>9</sub>S<sub>10</sub>); Tr: troilite (FeS); Pn: pentlandite, Mi: millerite; Vs: vaesite; Vi: violarite; Gd:  
1081 godlevskite; Hz: heazlewoodite.

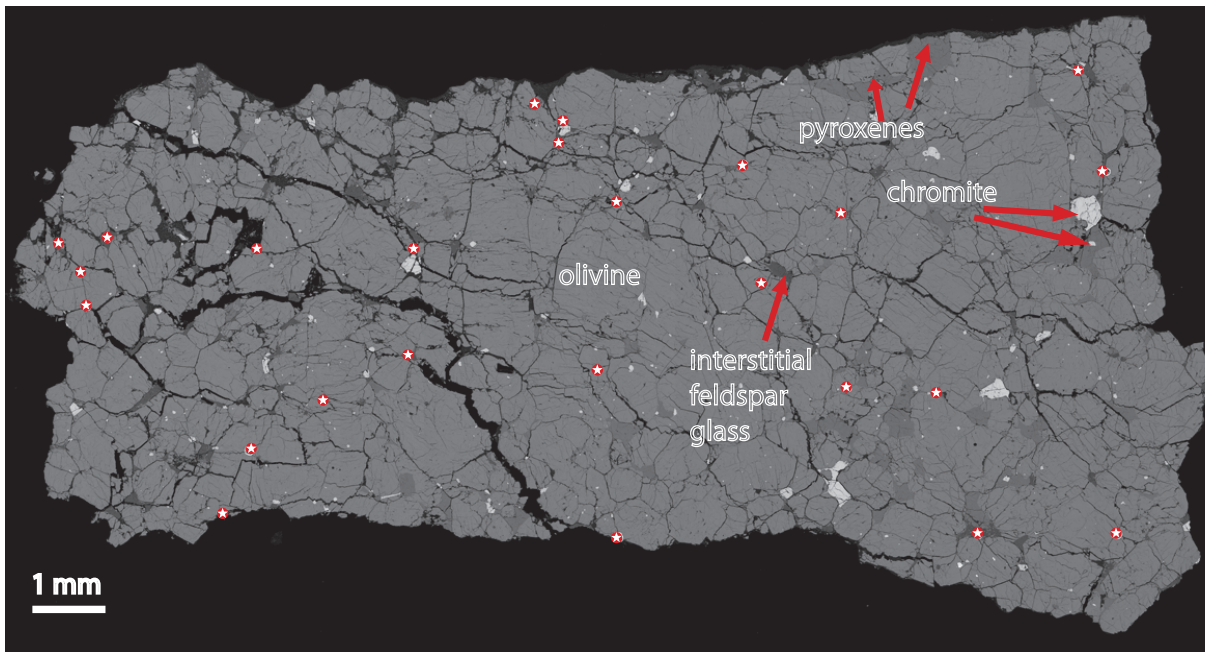
1082

1083 FIGURE 10: Log  $fS_2$  vs. log  $fO_2$  diagram for the Fe-S-O system at 800°C (after Parat et al., 2011).

1084 The compositional range of Chassigny pyrrhotite can coexist with anhydrite if the oxygen fugacity

1085 is above that defined by the synthetic assemblage FMQ (Fayalite-Magnetite-Quartz);  $Fe_7S_8$ :

1086 monoclinic pyrrhotite;  $Fe_9S_{10}$ : hexagonal pyrrhotite (Kissin and Scott, 1982).



1087

Fig. 1

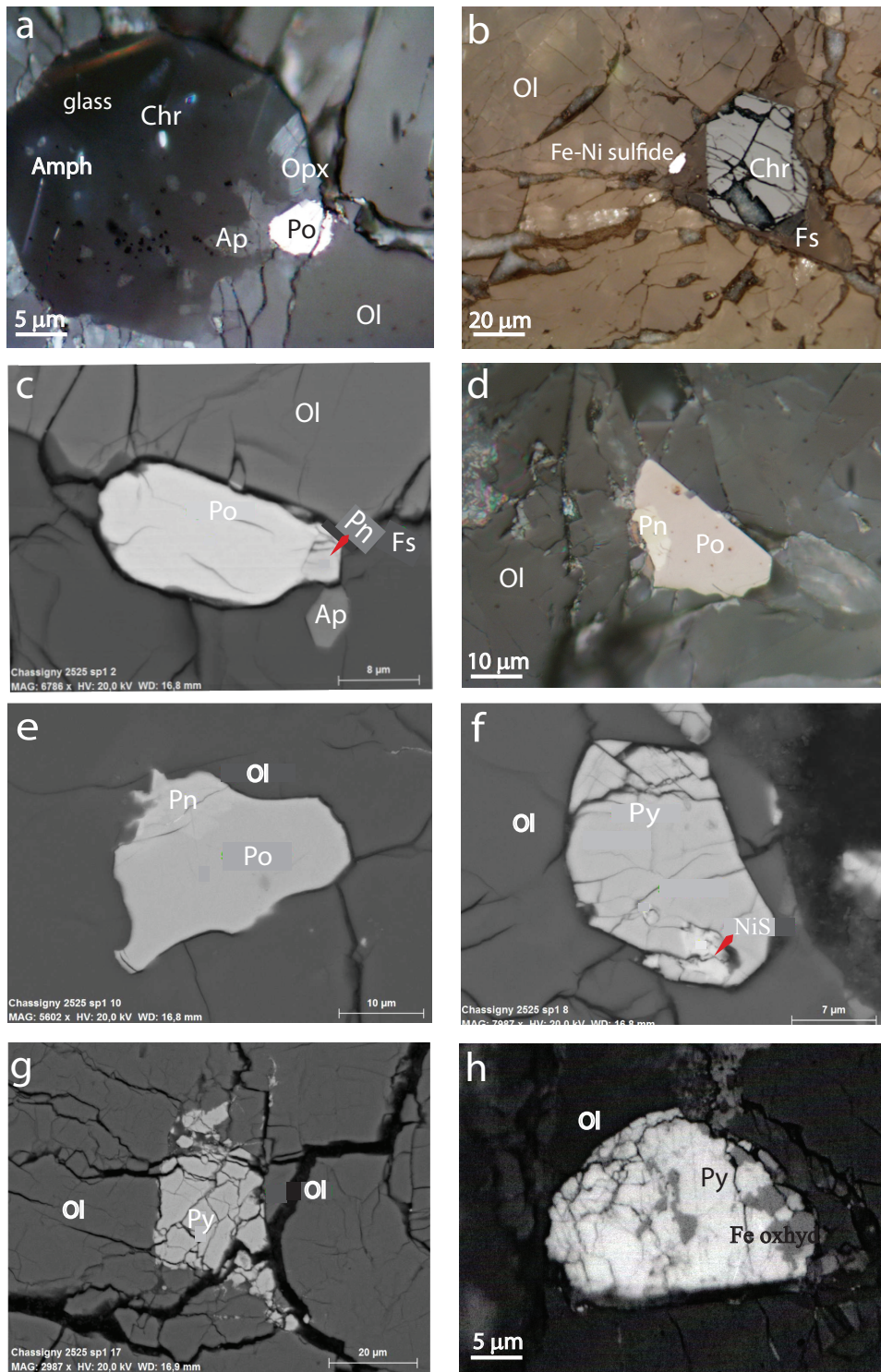


Fig. 2

Number of sulfide grains

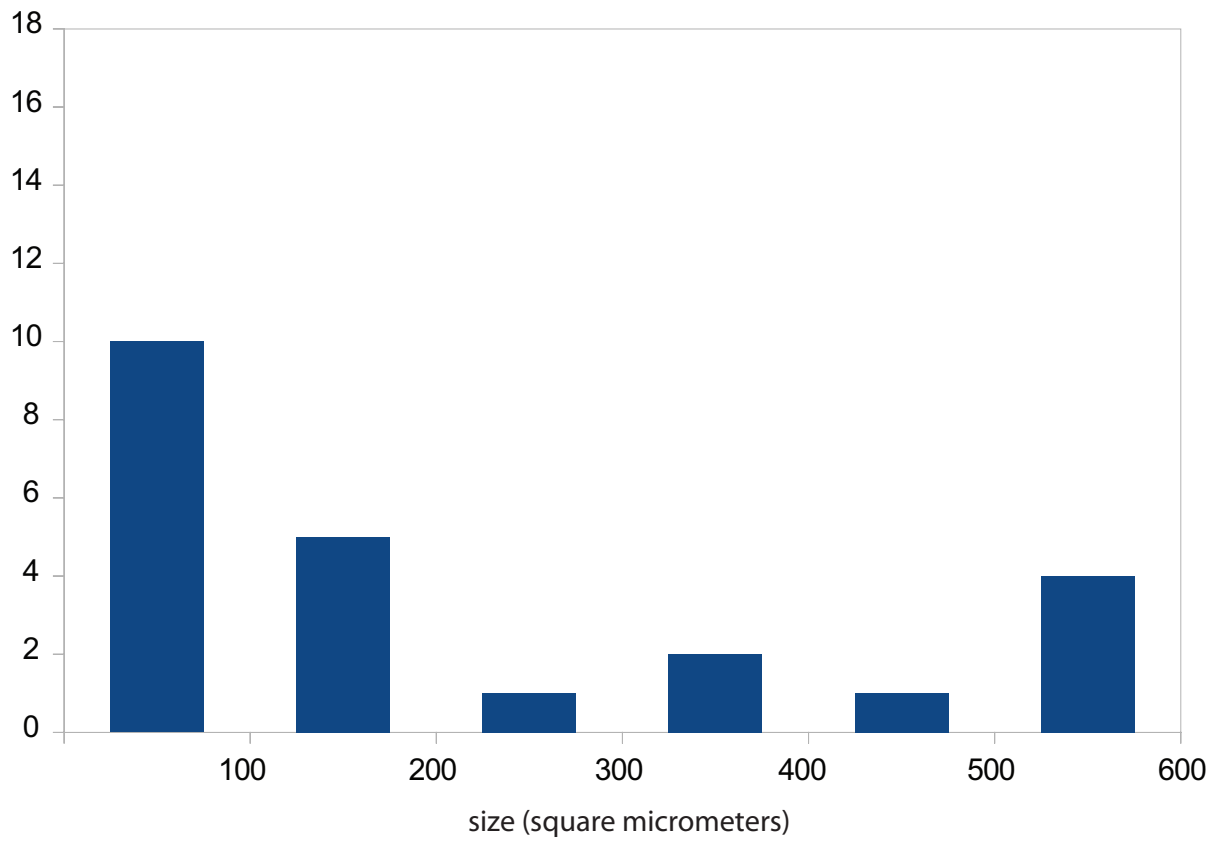


Fig. 3

number of analyses

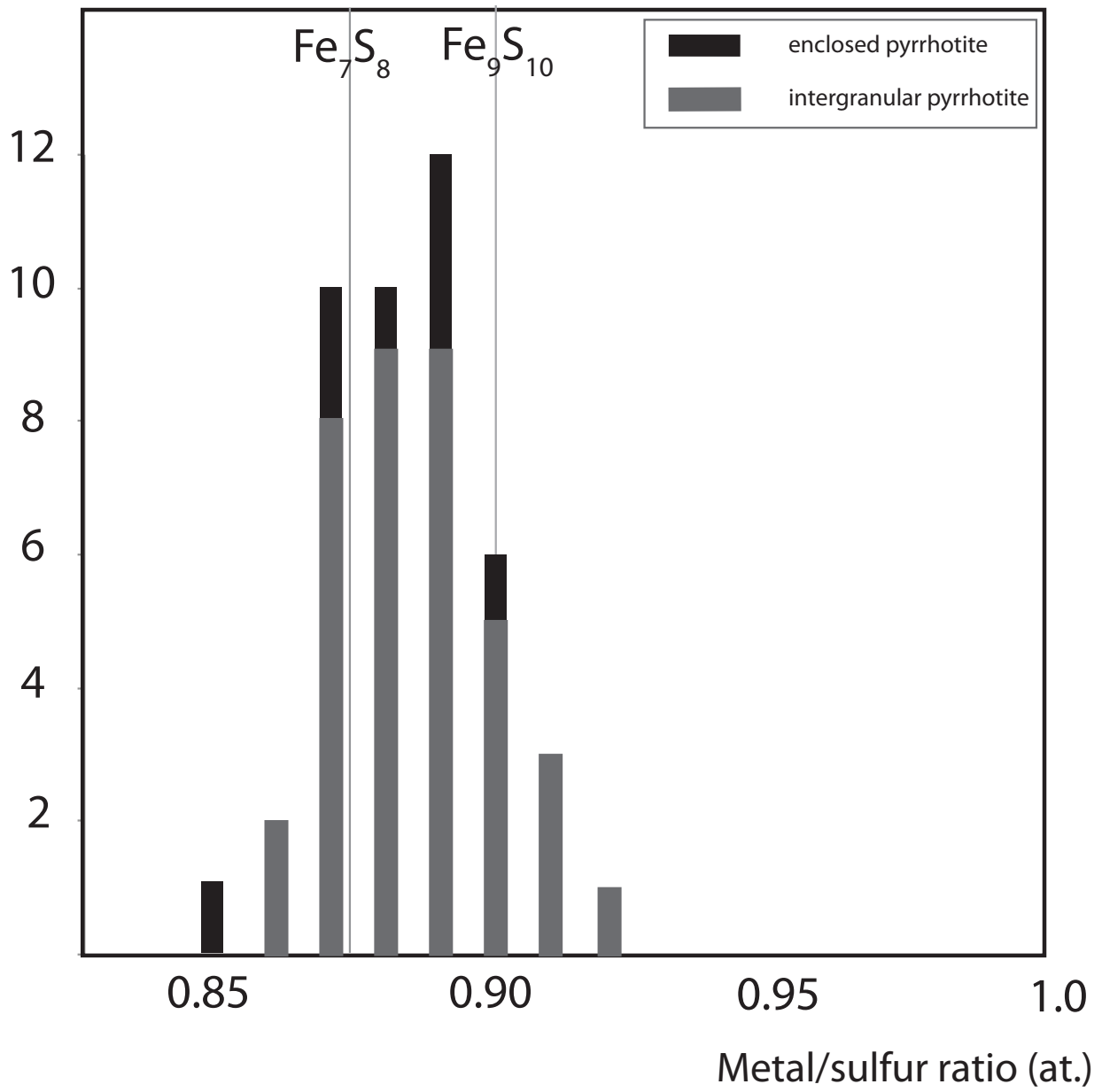


Fig. 4

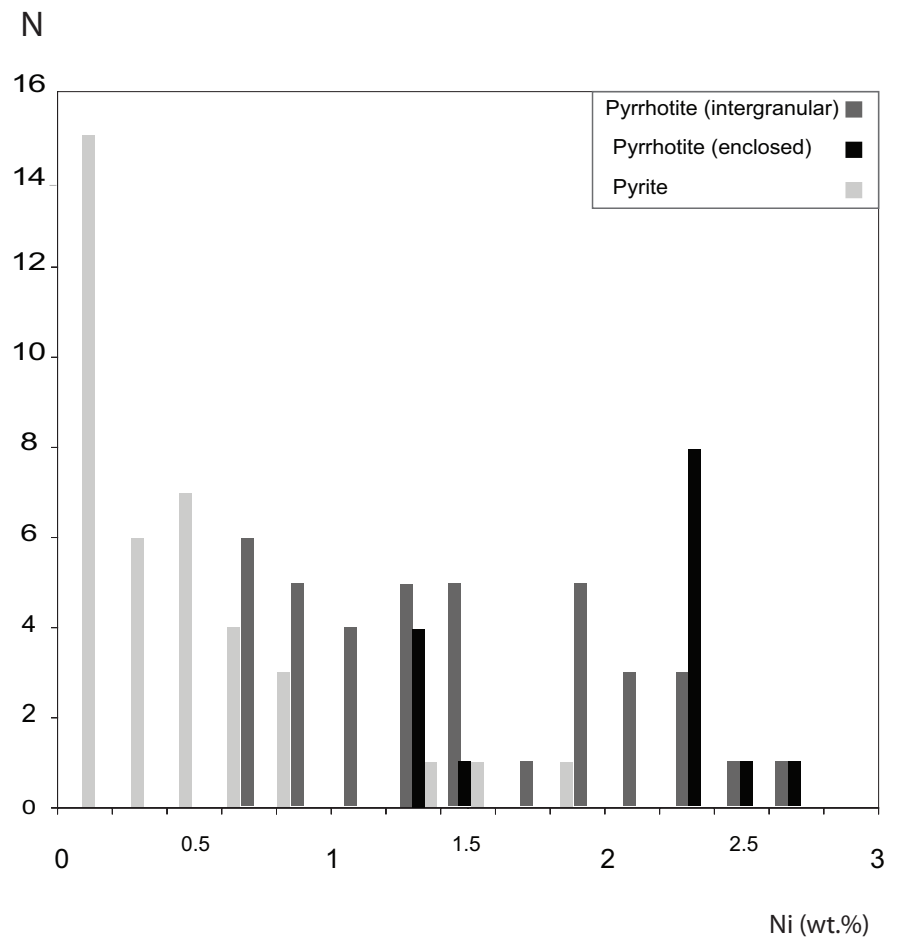


Fig. 5

metal/sulfur(at.)

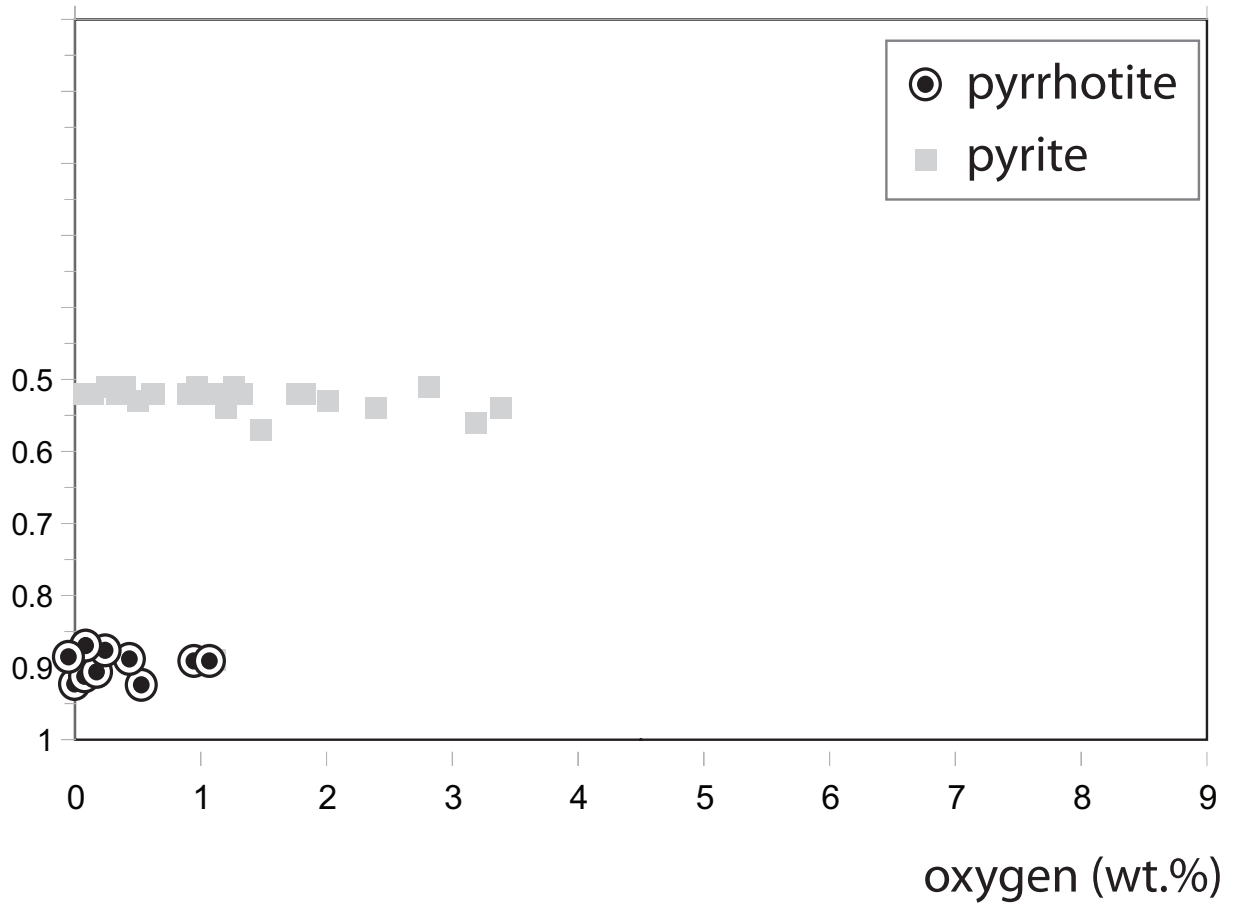


Fig. 6

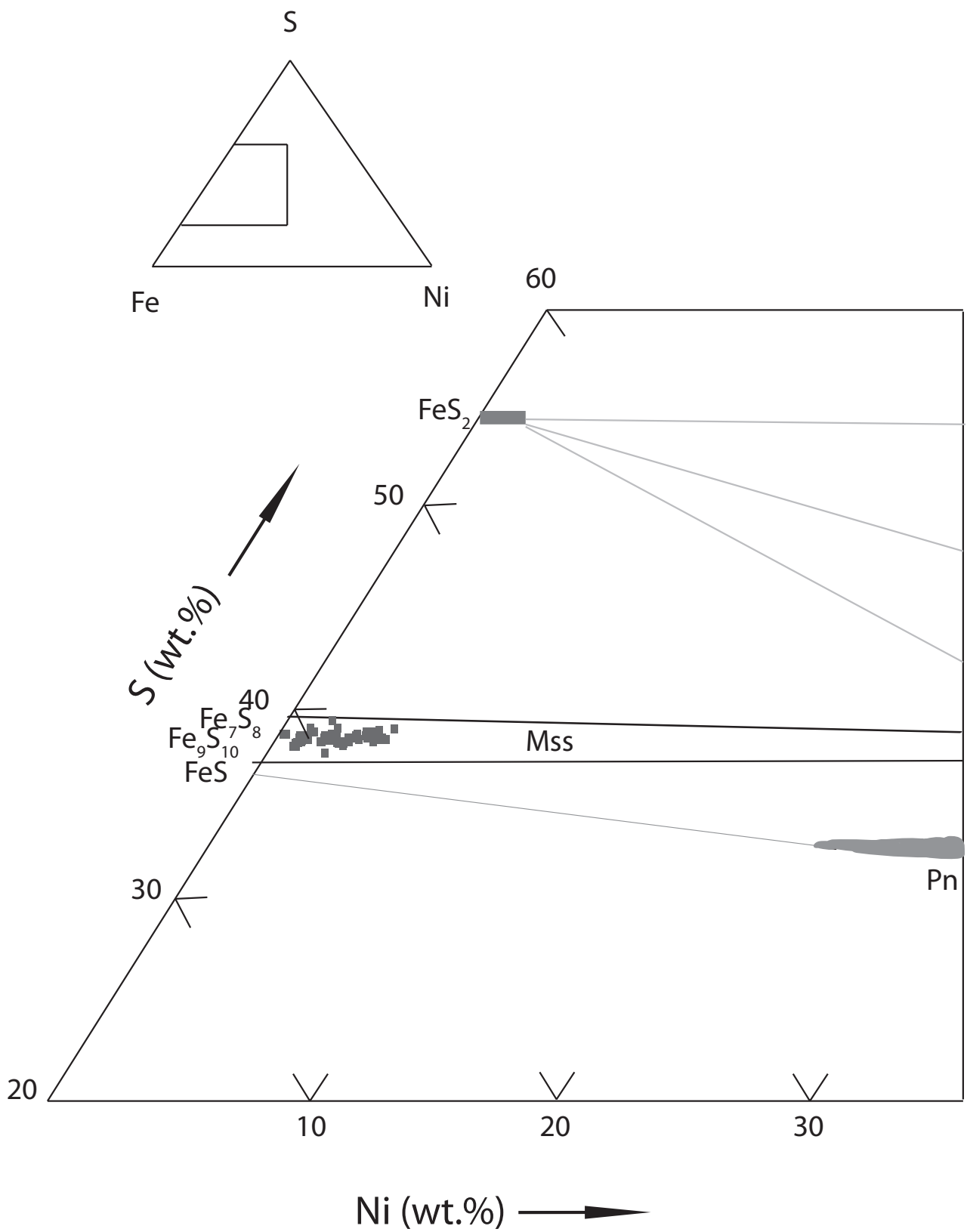


Fig. 7

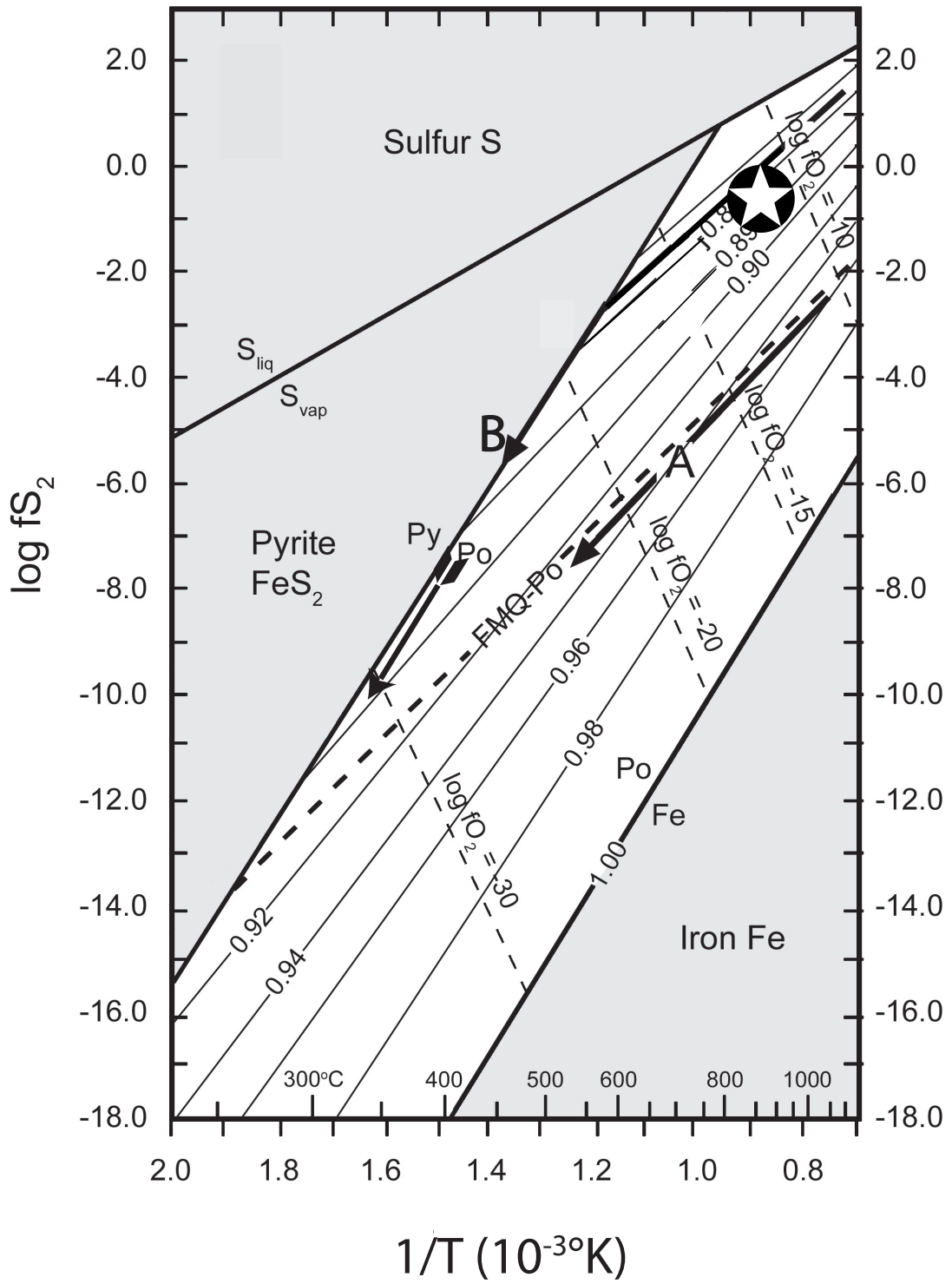


Fig. 8

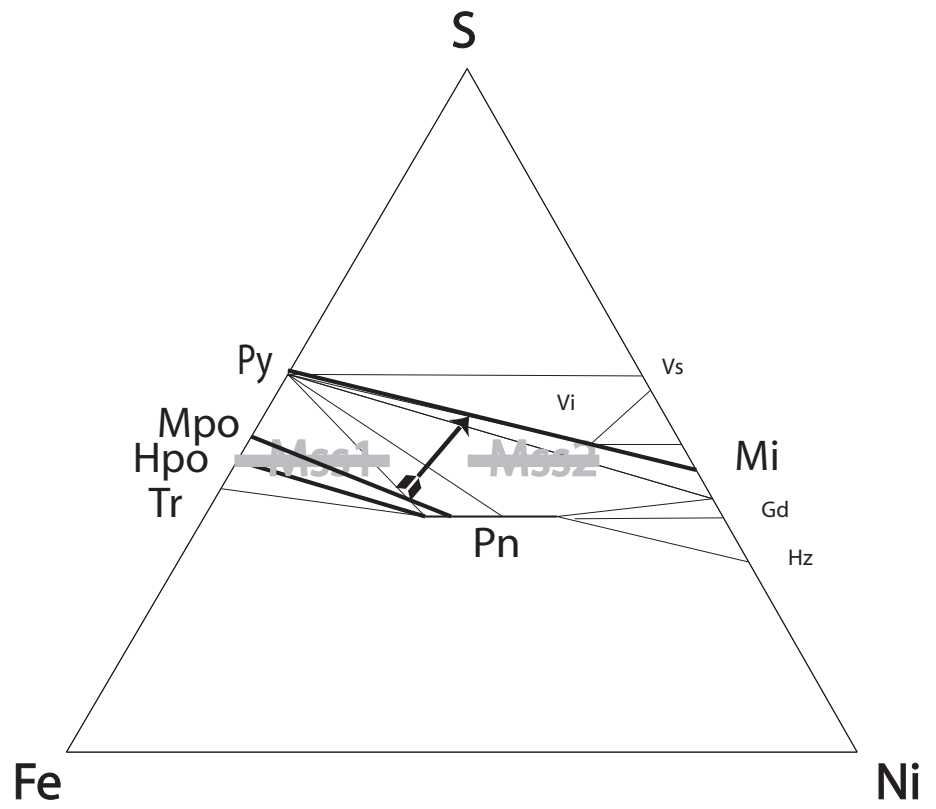


Fig. 9

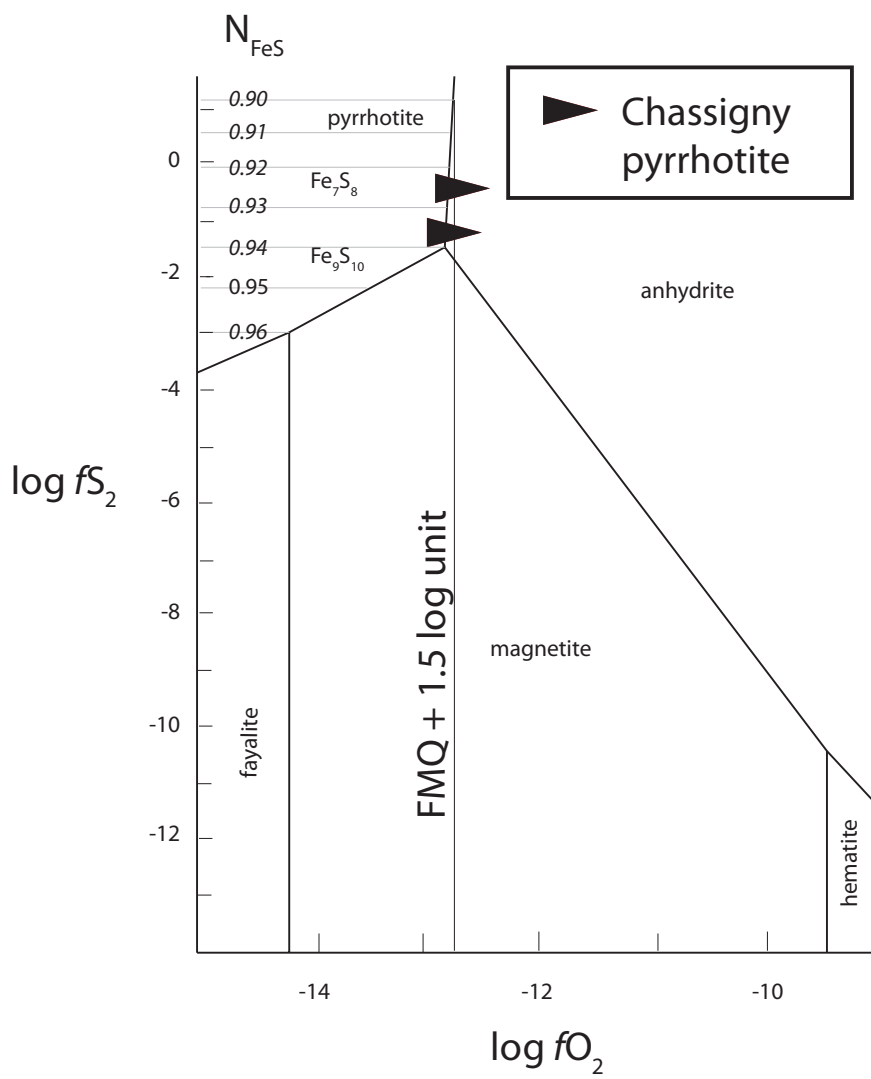


Fig.10

1099 **Table 1: Replicate analyses of Del Norte County troilite (Oregon, USA).**

1100

1101

1102

1103

1104

	(A) n = 5	(B) n = 36	(C) n = 10
wt%			
Fe	63.45 ± 0.05	63.43 ± 0.23	63.30 ± 0.30
Ni	-	-	-
Co	-	-	-
S	36.53 ± 0.03	36.56 ± 0.20	36.31 ± 0.20
total	99.98	99.99	99.61
M/S	0.999	0.998	1.000
	SEM	EMP	EMP

1111

1112

1113

1114

1115

1116 A : Gattaceca et al. (2013), B : Chevrier et al. (2011), C : Lorand et al. (2012). = : number of analyses. M/S :  
 1117 metal/sulfur atomic ratio (M = Fe+Ni+Co). - : below detection limit (<0.05 wt%). SEM : scanning electron microscope  
 1118 standardless procedure (Muséum National d'Histoire Naturelle, Paris); EMP : electron microprobe analysis  
 1119 (Camparis).  
 1120

**Table 2: Representative analyses of Fe-Ni sulfides from the Chassigny meteorite**

<b>mineral sulfide grain</b>	E Po Po5113	E Po Pod10	E Po Pod10	I Po Pod11	I Po Pod11	I Po Pod11	I Po Po3h2
wt%							
Fe	59.08	56.15	58.0	57.73	57.27	58.24	58.51
Ni	1.5	2.77	2.54	2.52	2.62	2.50	2.37
Co	-	0.09	-	-	-	-	0.26
Cu	-	-	0.15	-	-	0.17	-
Mn	-	0.1	-	-	-	0.05	-
Zn	-	-	-	0.08	-	-	-
S	38.8	39.78	39.1	39.57	39.67	39.17	39.60
O	-	-	-	na	na	0.20	0.18
Total	99.38	98.89	97.79	99.90	99.56	100.34	100.92
M/S	0.89	0.87	0.88	0.88	0.88	0.89	0.88
<b>mineral sulfide grain</b>	I Po Po3h2	I Po Po3h2	I Po Po1a16	I Po Po1a16	I Po Po1a16	I Po Po7C10	*I Pn Po1a16
wt%							
Fe	58.02	58.14	58.8	60.45	59.57	60.65	32.88
Ni	2.35	2.14	1.75	1.4	2.0	1.03	32.94
Co	0.05	0.17	0.2	-	-	-	-
Cu	-	-	-	-	0.15	-	-
Mn	-	-	-	-	-	-	-
Zn	-	0.08	-	-	-	-	-
S	39.62	39.22	38.6	39.36	39.16	38.80	34.18
O	0.08	na	na	0.05	0.07	0.07	na
Total	100.12	99.75	99.41	101.26	100.95	100.55	100.0
M/S	0.88	0.875	0.90	0.88	0.89	0.91	1.08
<b>mineral sulfide grain</b>	I Py Pyb7	I Py Py6e17	I Py	I Py	I Py	I Py	*I Mi
wt%							

Fe	46.57	45.54	47.28	46.23	45.35	44.24	3.89
Ni	0.1	0.94	0.46	0.46	1.49	0.53	61.89
Co	-	-	-	-	-	0.11	-
Cu	0.05	-	-	-	0.06	0.05	-
Mn	-	-	-	-	-	-	-
Zn	-	-	-	0.18	0.49	0.90	-
S	53.23	53.91	52.37	51.7	48.65	48.07	34.5
O	na	na	0.63	1.19	3.19	4.26	na
Total	99.94	100.39	100.74	99.66	99.13	98.16	99.28
M/S	0.5	0.51	0.54	0.52	0.56	0.53	1.04

E Po : enclosed pyrrhotite ; I Po : intergranular pyrrhotite ; I Pn : intergranular pentlandite  
I Py : intergranular pyrite ; I Mi ; intergranular millerite ; EMP analyses except \*  
(EDS analyses) ; na : not analysed ; - : below detection limits (<0.05 wt%).

1121

**Table 3: Electron microprobe analyses of Chassigny olivine**

	Mean (27 analyses)	Standard deviation
Wt%		
SiO <sub>2</sub>	37.40	0.26
TiO <sub>2</sub>	-	-
Al <sub>2</sub> O <sub>3</sub>	-	-
Cr <sub>2</sub> O <sub>3</sub>	-	-
FeO	28.1	0.26
MgO	34.13	0.38
MnO	0.50	0.15
NiO	0.06	0.03
CaO	0.13	0.03
Total	100.32	
Mg/Mg+Fe <sup>2+</sup> (at.)	0.68	

1122 - : below detection limit (<0.05 wt %)

1123

1124

1125

1126

1127

1128

1129

1130

1131

1132

1133

1134 **Table 4: Sulfide modal abundances and pyrrhotite compositions in Nakhrites and Chassignites.**

1135

1136

1137

1138

1139 **Nakhrites**

1140 NWA 817  $0.02 \pm 0.01^1$   $0.874 \pm 0.01^1$

1141 MIL nakhrites  $0.042^2$   $0.89^2-0.90^3$

1142 Yamato nakhrites  $0.86-0.88^4$

1143 Nakhla  $0.04 \pm 0.013^1$   $0.88 \pm 0.02^1$

1144  $0.88^5$

1145 Governador Valadares  $0.87^5$

1146  $0.037 \pm 0.012^1$   $0.88 \pm 0.016^1$

1147 Lafayette  $0.87^5$

1148 NWA 998  $0.08 \pm 0.03^1$   $0.881^1$

1149  $0.04^6$

1150 **Chassignites**

1151 Chassigny  $0.005^7$   $0.88 \pm 0.01^7$

1152 NWA 2737  $0.01 \pm 0.005^8$   $1.05^8$

1153

1154 1 : Chevrier et al (2011); 2 : Day et al. (2006), 3 : Frantz et al., (2014); 4 : Imae and Ikeda (2007); 5 : Greenwood et al.  
 1155 (2000a); 6 : Irving and Treiman (2008); 7 : This study; 8 : Lorand et al. (2012).

1156

1157